GLOBAL BIOGEOCHEMICAL CYCLES, VOL. 18, GB4028, doi:10.1029/2004GB002220, 2004

Upper ocean ecosystem dynamics and iron cycling in a global three-dimensional model

J. Keith Moore
Earth System Science, University of California, Irvine, California, USA

Scott C. Doney
Department of Marine Chemistry and Geochemistry, Woods Hole Oceanographic Institution, Woods Hole, Massachusetts, USA

Keith Lindsay
Oceanography Section, National Center for Atmospheric Research, Boulder, Colorado, USA

Received 2 January 2004; revised 6 August 2004; accepted 8 September 2004; published 14 December 2004.

[1] A global three-dimensional marine ecosystem model with several key phytoplankton functional groups, multiple limiting nutrients, explicit iron cycling, and a mineral ballast/organic matter parameterization is run within a global ocean circulation model. The coupled biogeochemistry/ecosystem/circulation (BEC) model reproduces known basin-scale patterns of primary and export production, biogenic silica production, calcification, chlorophyll, macronutrient and dissolved iron concentrations. The model captures observed high nitrate, low chlorophyll (HNLC) conditions in the Southern Ocean, subarctic and equatorial Pacific. Spatial distributions of nitrogen fixation are in general agreement with field data, with total N-fixation of 55 Tg N. Diazotrophs directly account for a small fraction of primary production (0.5%) but indirectly support 10% of primary production and 8% of sinking particulate organic carbon (POC) export. Diatoms disproportionately contribute to export of POC out of surface waters, but $CaCO_3$ from the coccolithophores is the key driver of POC flux to the deep ocean in the model. An iron source from shallow ocean sediments is found critical in preventing iron limitation in shelf regions, most notably in the Arctic Ocean, but has a relatively localized impact. In contrast, global-scale primary production, export production, and nitrogen fixation are all sensitive to variations in atmospheric mineral dust inputs. The residence time for dissolved iron in the upper ocean is estimated to be a few years to a decade. Most of the iron utilized by phytoplankton is from subsurface sources supplied by mixing, entrainment, and ocean circulation. However, owing to the short residence time of iron in the upper ocean, this subsurface iron pool is critically dependent on continual replenishment from atmospheric dust deposition and, to a lesser extent, lateral transport from shelf regions. *INDEX TERMS:* 0315 Atmospheric Composition and Structure: Biosphere/atmosphere interactions; 0322 Atmospheric Composition and Structure: Constituent sources and sinks; 1610 Global Change: Atmosphere (0315, 0325); 1615 Global Change: Biogeochemical processes (4805); *KEYWORDS:* ecosystem model, nutrient limitation, iron cycle, phytoplankton community

Citation: Moore, J. K., S. C. Doney, and K. Lindsay (2004), Upper ocean ecosystem dynamics and iron cycling in a global three-dimensional model, *Global Biogeochem. Cycles*, *18*, GB4028, doi:10.1029/2004GB002220.

1. Introduction

[2] Growing appreciation for the key roles played in ocean biogeochemistry by phytoplankton functional groups and trace metal limitation is leading to a new generation of more sophisticated, coupled ocean biological, chemical, and physical models [e.g., *Doney*, 1999; *Doney et al.*, 2001, 2003]. Here we present solutions from one such global three-dimensional (3-D) model developed by embedding the upper ocean ecosystem model of *Moore et al.* [2002a, 2002b] (METa and METb hereinafter, respectively) and an expanded version of the biogeochemistry module developed as part of the Ocean Carbon Model Intercomparison Project (OCMIP) [*Doney et al.*, 2001, 2003] into the ocean circulation component of the Community Climate System Model (CCSM) [*Gent et al.*, 1998; *Blackmon et al.*, 2001]. Our focus is on the skill of this coupled biogeochemistry/ecosystem/circulation (BEC) model at representing the observed basin-scale patterns of biomass, productivity,

0886-6236/04/2004GB002220$12.00

community structure, and carbon export as well as the sensitivities of those patterns to changes in external forcing (e.g., atmospheric dust/iron deposition).

[3] Shifts in the size-structure and composition of phytoplankton communities can strongly influence carbon cycling in surface waters and export to the deep ocean. Under strongly nutrient limiting conditions, ecosystems are often characterized by small pico- and nano-sized phytoplankton (more efficient at nutrient uptake than larger phytoplankton), strong grazing pressure from microzooplankton, high particulate organic carbon (POC) recycling, and low vertical carbon export. Larger phytoplankton, such as diatoms, typically grow quickly under light and nutrient replete conditions and experience less grazing pressure. Thus diatoms often dominate episodic blooms and are a major contributor to the POC sinking flux from surface waters [*Buesseler*, 1998]. Coccolithophores are another common component of blooms, particularly in temperate waters. These phytoplankton form external platelets of calcium carbonate ($CaCO_3$), a key process affecting carbonate cycling in the oceans that can influence surface water pCO_2 concentrations and air-sea flux [*Holligan et al.*, 1993; *Robertson et al.*, 1994]. The mineral ballast produced by diatoms and coccolithophores also may enhance carbon export to the deep ocean [*Armstrong et al.*, 2002; *Klaas and Archer*, 2002]. Diazotrophs, phytoplankton capable of fixing N_2 gas into more bioavailable nitrogen forms, represent a key source of new nitrogen in warm tropical/subtropical regions [*Karl et al.*, 1997; *Capone et al.*, 1997; *Karl et al.*, 2002; *Kustka et al.*, 2002].

[4] Each of these functional groups of phytoplankton is represented in our ecosystem module (METa; METb). Previously, we validated a version of the model running in a simple, surface layer physical framework against a diverse set of field observations from nine JGOFS and historical time series locations (METa), satellite observations, and global nutrient climatologies (METb). The simplified vertical treatment, absence of horizontal advection, and prescribed subsurface nutrient concentrations were limitations in these simulations, problems alleviated here in the full 3-D implementation. The BEC model includes explicit iron cycling with external sources to the oceans from mineral dust deposition and shallow water sediments. The importance of iron as a key regulator of phytoplankton growth and community structure in the oceans is well established, particularly for the high nitrate, low chlorophyll (HNLC) regions [i.e., *Martin et al.*, 1991; *Price et al.*, 1994; *de Baar et al.*, 1995; *Coale et al.*, 1996, *Landry*, 1997; *Boyd and Harrison*, 1999]. Basin- and global-scale ecosystem modeling studies have been published during the past decade, but most have not included iron as a limiting nutrient [i.e., *Sarmiento et al.*, 1993; *Six and Maier-Reimer*, 1996; *Oschlies and Garçon*, 1999; *Bopp et al.*, 2001; *Palmer and Totterdell*, 2001]. Iron cycling has been included in ecosystem local 1-D simulations [*Chai et al.*, 1996; *Loukos et al.*, 1997; *Leonard et al.*, 1999; *Lancelot et al.*, 2000] and has recently been included in a 3-D ecosystem and circulation model of the equatorial Pacific [*Christian et al.*, 2002] and in two global-scale simulations [*Aumont et al.*, 2003; *Gregg et al.*, 2003].

[5] Significant uncertainties surround the biogeochemical cycling of iron in the oceans [*Johnson et al.*, 1997; *Fung et al.*, 2000; *Johnson et al.*, 2002]. *Johnson et al.* [2002] summarize a number of outstanding questions regarding the effects of speciation, organic ligands, and bioavailability; cellular and detrital iron quotas (i.e., Fe/C ratios); factors that control the rates of adsorption to particles (abiotic scavenging); and the magnitude of external sources of iron from mineral dust deposition/dissolution and ocean sediments. In order to simulate the ocean iron cycle, we have had to make simplifying assumptions in regard to each of these issues. For example, we assume that the dissolved iron pool is completely bioavailable to all phytoplankton without regard to speciation or ligand dynamics. These assumptions are necessary at present to begin to incorporate iron dynamics into models of ocean biogeochemistry. However, we recognize that many of the key processes are crudely parameterized and may need to be modified as understanding improves.

[6] In this work, our emphasis is on annual ecosystem dynamics, carbon fluxes, and iron biogeochemistry in the upper few hundred meters of the water column at the global scale. Results are presented from an initial 24-year control simulation and several sensitivity experiments. Simulated upper ocean nutrient concentrations and ecosystem dynamics approach a relatively stable, repeating seasonal cycle, after $\sim$10 years, and we present results from the final year. The timescale for the deep ocean to reach dynamical equilibrium is much longer, on the order of several thousand years, and the interaction of the coupled model on deep ocean nutrients will be a focus of future work. Similarly, we will address seasonal timescale variations in phytoplankton biomass and nutrient limitation and detailed comparisons between the model output and field data collected at the JGOFS and historical time series locations elsewhere.

2. Methods

2.1. Ecosystem Implementation

[7] The ecosystem model includes the nutrients nitrate, ammonium, phosphate, dissolved iron (dFe), and silicate (dSi); four phytoplankton functional groups; one class of zooplankton; dissolved organic matter (DOM); and sinking particulate detritus. Coccolithophores (and $CaCO_3$ production) are included implicitly as a variable fraction of the small phytoplankton group. The ecosystem model and its behavior in a global surface mixed-layer model are described in detail in METa and METb. Here we focus on differences between this implementation and METa. For further details the reader is referred to METa.

[8] The original ecosystem model allows for variable elemental ratios in all components of the ecosystem, and phytoplankton growth is modeled according to a dynamic growth (internal cellular quota) parameterization based on work by *Geider et al.* [1998]. The current model assumes fixed C/N/P elemental ratios within phytoplankton groups and zooplankton, and a fixed Fe/C ratio in zooplankton, significantly reducing the number of advected tracers and computational costs. Phytoplankton Fe/C ratios and diatom Si/C ratios are allowed to vary based on ambient nutrient

Table 1. Key Parameters Used in the Marine Ecosystem Portion of the Coupled BEC Model[a]

Value	Parameter
0.02	fraction of atmospheric iron deposition which dissolves at surface
3.0[b]	maximum C-specific growth rates for diatoms and sphyto
0.4[b]	maximum C-specific growth rate for diazotrophs
0.1	nongrazing mortality term for diatoms and sphyto
0.18	nongrazing mortality term for diazotrophs
0.009	coefficient in quadratic mortality/aggregation term for diatoms and sphyto
2.75[b]	maximum grazing rate on sphyto
2.0[b]	maximum grazing rate on diatoms
1.2[b]	maximum grazing rate on diazotrophs
0.1[b]	linear zooplankton loss term
0.46[b]	quadratic zooplankton loss term
1.05	coefficient z_grz used in zooplankton grazing rate calculation
0.01	inverse timescale of DOM remineralization (100 days)
0.5	Ks value for sphyto nitrate uptake
2.5	Ks value for diatom nitrate uptake
0.005	Ks value for sphyto ammonium uptake
0.08	Ks value for diatom ammonium uptake
1.0	Ks value for diatom silicate uptake
0.0003125	Ks value for sphyto phosphate uptake
0.005	Ks value for diatom phosphate uptake
0.0075	Ks value for diazotroph phosphate uptake
60	Ks value for sphyto iron uptake (pM)
160	Ks value for diatom iron uptake (pM)
100	Ks value for diazotroph iron uptake (pM)
0.25	initial slope of P vs. I curve for diatoms and sphyto (see METa)
0.028	initial slope of P vs. I curve for diazotrophs
6.0	optimum Fe/C ratio (μmol/mol) for diatoms and sphyto
2.5	minimum Fe/C ratio (μmol/mol) for diatoms and sphyto
2.5	fixed Fe/C ratio (μmol/mol) for zooplankton
48.0	optimum Fe/C ratio (μmol/mol) for diazotrophs
14.0	minimum Fe/C ratio (μmol/mol) for diazotrophs
0.137	optimum Si/C ratio (mol/mol) for diatoms
0.685	maximum Si/C ratio (mol/mol) for diatoms
0.0685	minimum Si/C ratio (mol/mol) for diatoms
0.137	fixed molar N/C ratio for all phytoplankton and zooplankton
0.00855	fixed molar P/C ratio for diatoms, sphyto, and zooplankton
0.00304	fixed molar P/C ratio for diazotrophs
2.3	maximum Chl/N ratio for (mg Chl/mmolN) for sphyto
3.0	maximum Chl/N ratio for (mg Chl/mmolN) for diatoms
3.4	maximum Chl/N ratio for (mg Chl/mmolN) for diazotrophs

[a]See *Moore et al.* [2002a] for details. Rates are daily unless noted otherwise. Concentrations are in μM unless noted otherwise. Term "sphyto" denotes small phytoplankton group.
[b]Parameter is scaled by the temperature function.

concentrations. We simulate explicit C, Fe, and chlorophyll pools for each phytoplankton group, and an explicit Si pool for diatoms. Phytoplankton growth is parameterized according to a balanced growth model with C/N/P ratios at modified Redfield values (117/16/1) for diatoms, small phytoplankton, zooplankton, and sinking detritus based on work by *Anderson and Sarmiento* [1994]. The ratio for diazotrophs is set at 329/45/1 to reflect the high C/P ratios observed for Trichodesmium (N/P of 45 [*Letelier and Karl*, 1996]), with the same C/N ratio as the other groups. All elemental ratios are allowed to vary within DOM.

[9] Phytoplankton growth rates are set by modifying the maximum growth rate for each functional group by whichever nutrient is most limiting for that group (lowest concentration relative to uptake half-saturation constants) and light. These limitations are multiplicative so phytoplankton can be light-nutrient colimited. Chlorophyll content and photoadaptation are based on work by *Geider et al.* [1998] with some modifications (METa). A temperature relationship with a q_{10} factor of 2.0 [*Doney et al.*, 1996] is used that reduces rates more strongly at low temperatures than in METa. This improves seasonal patterns of production and biomass at high latitudes. Ecosystem parameters are listed in Table 1.

[10] Model phytoplankton are allowed to adapt to low available iron levels with some plasticity in their Fe/C ratios [*Sunda and Huntsman*, 1995, 1997]. Variable Fe/C ratios are implemented by subtracting iron due to phytoplankton loss terms (e.g., grazing, mortality) at the current Fe/C ratio (Qfe) for each group and then adding new biomass at a growth Fe/C ratio (gQfe) determined by ambient iron concentrations and the iron uptake half-saturation constant for each group. Optimum Fe/C ratios (Qfe_{opt}) are set for each group and are used when dissolved iron is plentiful relative to the half-saturation constant ($dFe > 2 \times Kfe$). These optimum ratios are 6 μmol/mol for diatoms and small phytoplankton (METa) and 48 μmol/mol for diazotrophs [*Berman-Frank et al.*, 2001; *Kustka et al.*, 2002, 2004]. As dFe falls below two times the half-saturation constant, the growth Fe/C ratio is reduced as $gQfe = Qfe_{opt} \times dFe/(2 \times Kfe)$. A minimum

Fe/C ratio of 2.5 μmol/mol is imposed for diatoms and small phytoplankton, and a minimum of 14 μmol/mol is set for diazotrophs [*Kustka et al.*, 2002]. Some phytoplankton species are capable of luxury uptake of iron, leading to high Fe/C ratios, but luxury uptake is not included. A fixed Fe/C of 2.5 μmol/mol is set for zooplankton, and if grazed material has higher Fe/C ratios, the excess is released as dissolved iron.

[11] Diatom Si/C and Si/N ratios increase under iron-stressed conditions [*Takeda*, 1998; *Hutchins et al.*, 1998], possibly linked to reduced growth rate through the cell cycle [*Martin-Jézéquel et al.*, 2000]. Diatoms also can significantly reduce their silicification levels under silicon-limited conditions [*Ragueneau et al.*, 2000]. We allow for both adaptations in the model with variable Si/C ratios implemented in a manner similar to Fe/C. An optimum Si/C ratio (Qsi_{opt}) of 0.137 (mol/mol) is used under nutrient-replete conditions [*Brzezinski*, 1985]. When iron uptake is limited by available dFe and silicate uptake is not, the Si/C ratio for new biomass is increased up to a maximum value of 0.685, according to $gQsi = (Qsi_{opt} \times Kfe/dFe) \times 5.0) - 0.2$. This results in a steep increase in Qsi as iron decreases, reaching the maximum value when dFe = 0.13 nM. If dissolved silicate uptake is significantly limited ($dSi < 2.0 \times Ksi$), then Si/C is not increased under low iron, and the growth Si/C ratio decreases as $gQsi = Qsi_{opt} \times dSi/(2.0 \times Ksi)$, to a minimum value of 0.0685. *Aumont et al.* [2003] utilized a somewhat similar parameterization of a variable Si/C ratio, reduced under low Si and increased under low ambient iron concentrations.

[12] Calcification is parameterized in a manner similar to METa based on the known ecology and global distributions of coccolithophores [*Iglesias-Rodríquez et al.*, 2002]. The base calcification rate ($CaCO_{3prod}$), set at 2.4% of the small phytoplankton primary production rate, is adjusted downward under nutrient-limited or low-temperature conditions. We decrease the production of $CaCO_3$ at low temperatures based on observations that coccolithophores are rarely found in cold polar waters. *Iglesias-Rodríguez et al.* [2002] found that coccolithophore blooms were most often observed at temperatures between 5° and 15°C in satellite data, and were rarely found south of the Antarctic Polar Front (PF) in the Southern Hemisphere. Summertime temperatures at the poleward edge of the PF are typically ~3°C [*Moore et al.*, 1999]. Thus we progressively reduce the calcification rate as temperatures fall below 5°C as $CaCO_{3prod} = CaCO_{3prod} \times (TEMP + 2.0)/7.0$. We decrease calcification under strongly nutrient-limiting conditions and increase calcification when the small phytoplankton group is blooming to try and capture the community composition typically associated with these conditions in the field. When nutrients are scarce, coccolithophores will tend to be outcompeted by smaller picoplankton that are more efficient at nutrient uptake. Coccolithophores are often a dominant component of non-diatom blooms, particularly in midlatitude temperate regions [*Iglesias-Rodríquez et al.*, 2002]. Thus, under bloom conditions, when the small phytoplankton biomass exceeds 3.0 μM carbon, the calcification rate is increased (up to a maximum of 40% of the small phytoplankton primary production) as $CaCO_{3prod} = CaCO_{3prod} \times (sphytoC/3.0)$. Currently, the model does not explicitly include calcification by other organisms.

[13] A single zooplankton pool grazes on all phytoplankton groups, with grazing parameters and the routing among remineralization and the detrital pools varying depending on the type of prey being consumed (METa). Thus our single zooplankton class is able to capture some ecological aspects of both microzooplankton and macrozooplankton. Fieldwork suggests that small phytoplankton experience much stronger grazing pressure from microzooplankton than do the other phytoplankton groups [i.e., *Sherr and Sherr*, 1988]. Maximum grazing rates are set higher for the small phytoplankton group, though parameters are such that it is possible for them to escape grazing control and bloom under optimal growth conditions. Grazing rates are lower and more material is routed to sinking detritus when diatoms are eaten, reflecting generally larger predators (e.g., copepods) and sinking fecal pellet production. Appendix A gives details of the routing of materials from phytoplankton and zooplankton mortality: between sinking particulate organic matter, suspended/dissolved organic matter, and remineralization to inorganic nutrient pools.

2.2. Remineralization of Detrital Pools

[14] The suspended/dissolved organic matter pool (DOM) in the oceans can be broken into roughly three components: a labile pool that is remineralized quickly on a timescale of hours to days, a semilabile pool that is remineralized on a timescale of months, and a refractory pool that has a lifetime of decades to thousands of years and accounts for the large DOM concentrations in the deep ocean [i.e., *Carlson*, 2002]. In the model, the labile DOM pool generated by, for example, phytoplankton excretion is instantly remineralized to inorganic nutrients. The remaining production of DOM is assumed to be semilabile and remineralizes with a lifetime of ~100 days. Thus, semilabile DOM can build up in surface waters over seasonal timescales and be exported from the euphotic zone. The 100-day timescale was chosen to give reasonable seasonal buildups of DOC given our particular routing of materials between instant remineralization, dissolved organic pools, and sinking particulate detrital pools (see Appendix A). As we ignore the refractory portion of the DOM pool, little DOM is exported to deep waters, and deep ocean concentrations are negligible. The treatment of DOM in the model is admittedly crude at present. Future work will seek to improve the representation of DOM.

[15] Sinking detrital organic and mineral ballast pools instantly sink and remineralize at depth in the same grid point where they originate. Fast-sinking particles could not advect far from their source location due to slow current speeds at depth and our coarse resolution. As the sinking particulate pool is now implicit, it is not grazed by zooplankton as in METa. Remineralization at depth is prescribed based on the mineral ballast model of *Armstrong et al.* [2002]. Organic matter entering the sinking detrital pool is divided into a "free" organic fraction (easily remineralized) and a mineral ballast associated fraction, which remineralizes deeper in the water column with the corresponding mineral dissolution. A portion of each mineral ballast (and

Table 2. Parameter Values Used in the Mineral Ballast Model of Particulate Remineralization Through the Water Column[a]

	Length, m	%Hard	OCRatio
Soft POM (C, N, P, Fe,)	70–643[b]	–	–
Biogenic Si	70–643[b]	60	0.035
$CaCO_3$	600	60	0.07
Mineral dust	600	95	0.07

[a]Values based on *Armstrong et al.* [2002] and *Klaas and Archer* [2002]. Length is the lengthscale of remineralization for the soft portion of ballast and associated POM, %Hard is the fraction assumed resistant to remineralization, and OCRatio is the assumed bound organic carbon/mineral ballast ratio by weight. A portion of the POM is bound to each mineral ballast and has the same remineralization profile as the ballast. The hard portion of each ballast and the associated POM remineralize with a long length scale of 40,000 m (see text for details).

[b]Parameter is scaled by our temperature function, range given for 30° to −2°C.

its associated POM) is assumed to be fast sinking and resistant to degradation and thus to sink to the bottom of the ocean before remineralization.

[16] Mineral ballast consists of dust from the atmosphere, $CaCO_3$ from the coccolithophores, and biogenic silica (bSi) from the diatoms. Three parameters are set for each ballast type: (1) the mass ratio of associated organic carbon/mineral ballast; (2) the ballast dissolution length scale of the "soft" ballast fraction; and (3) the "hard" ballast fraction that mostly dissolves in the bottom model cell (assigned a very long, but not infinite, remineralization length scale of 40,000 m in our simulations). In addition, there is a remineralization length scale for the "free" POM. The organic carbon/mineral ballast mass ratios are based largely on the sediment trap analysis of *Klaas and Archer* [2002]. The remineralization length scales for "free" POM and bSi increase with decreasing water temperature using the temperature rate function from the ecosystem model. The dissolution of bSi is known to be strongly influenced by temperature, and significantly steeper temperature functions have been used [e.g., *Gnanadesikan*, 1999]. The mineral ballast model parameter values are presented in Table 2. The sinking detrital pool has variable dust/bSi/CaCO3/C/Fe ratios with C/N/P fixed at Redfield values. As described in Appendix S, 10% of scavenged iron is added to this sinking pool. Dissolved iron is released as portions of the sinking dust pool dissolve/remineralize at depth, assuming an iron content of 3.5% by weight. The current simulations are too short to examine how the mineral ballast model influences deep ocean nutrient distributions over long timescales.

2.3. Iron Cycling

[17] We make a number of simplifying assumptions to incorporate iron dynamics. All dissolved iron is assumed available for uptake by phytoplankton with no regard for speciation or ligand interactions. In META, nutrient concentrations below the surface mixed layer were held constant. Iron scavenging rates were set high where dissolved iron exceeded 0.6 nM, the high dust deposition regions, and at a low background rate elsewhere. Initial experiments with the 3-D model showed that this background rate was much too low, leading to a rapid buildup of dissolved iron in the upper few hundred meters of the water column in many regions. It is this scavenging onto particles and subsequent removal that keeps subsurface nutrient pools deficient in iron relative to macronutrients. Thus, scavenging rates for dissolved iron have been increased significantly over those in META and are parameterized as a more complicated function of sinking particle flux (dust and particulate organic carbon (POC)), standing particle concentration (POC pools), and the ambient iron concentration (see Appendix A).

[18] The model is forced with a simulated dust climatology, over the period 1979–2000, validated against measurement sites around the globe [*Luo et al.*, 2003]. The fraction of iron that dissolves upon surface dust deposition is uncertain and likely varies depending on atmospheric processing and deposition pathway (wet versus dry) [*Jickells and Spokes*, 2001], but little information is available at present to develop a global parameterization [*Fung et al.*, 2000]. Dust iron content and surface solubility are therefore set at fixed values of 3.5% iron by weight and 2.0%, respectively. In prior modeling efforts, iron release is assumed to occur only in surface waters [*Archer and Johnson*, 2000; *Christian et al.*, 2002; *Moore et al.*, 2002a, 2002b; *Aumont et al.*, 2003]. However, further dissolution/iron release may happen deeper in the water column as the result of slow dissolution from fast sinking dust particles/aggregates or consumption of dust particles by grazers, where a substantial release of iron is likely due to low pH levels in the gut [*Barbeau et al.*, 1996]. To account for these processes, an additional 3% of the dust is prescribed to dissolve within the water column with a remineralization length scale of 600 m. We make this somewhat arbitrary assumption based on the idea that the likelihood of a dust particle passing through an animal gut is greatest in the upper water column and decreases at greater depths, following the general vertical distribution of grazer biomass. The remaining dust/iron remineralizes with a long length scale as described above for ballast materials (40,000 m). Sinking dust particles also act to scavenge dissolved iron and remove it to the sediments (Appendix A). In the upper ocean, the scavenging due to dust is small in most regions compared with that due to biogenic particles. However, in the deep ocean, sinking dust particles account for a significant fraction of total scavenging in the model.

[19] Sediments are an important source of dissolved iron to oceanic waters [*Johnson et al.*, 1999; *de Baar and de Jong*, 2001], but little quantitative information is available for parameterizations of this process. In META, we set the fixed subsurface iron concentrations higher in shallow regions to account for this source. *Johnson et al.* [1999] estimated a diffusive flux out of the sediments in the coastal upwelling system off California (a high productivity region) at 5 μmol Fe/m^2/day, noting that the iron flux from sediment resuspension was likely even larger. As a first, admittedly crude attempt, we include a uniform sediment iron source of 2 μmol Fe/m^2/day for areas where depth is less than 1100 m. Inputs are likely too low in shallow, highly productive regions and too high in deeper areas underlying lower productivity waters. However, even this simple parameterization notably improves the model results in several

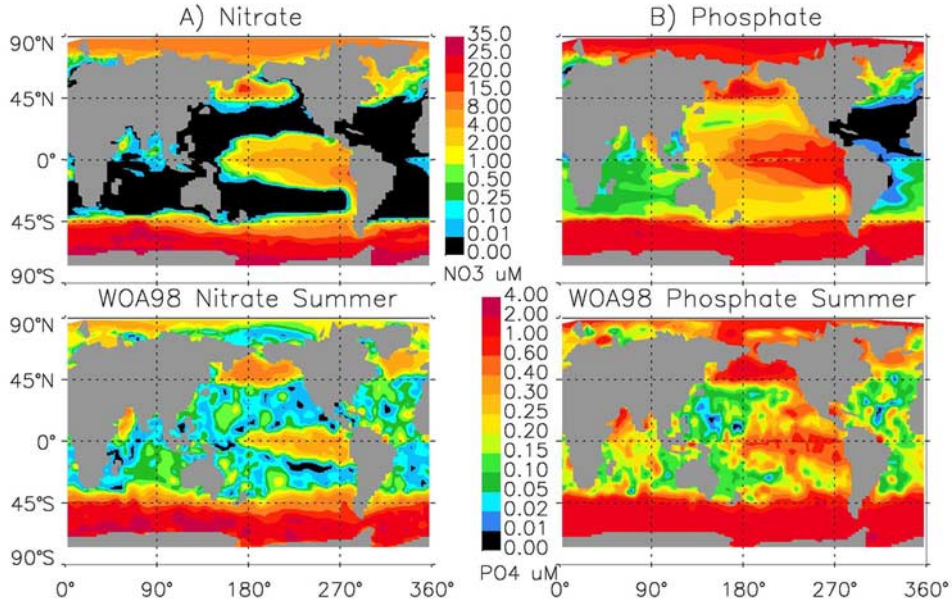

Figure 1. Surface nitrate and phosphate concentrations (summer season in each hemisphere) are compared with climatological concentrations from the World Ocean Atlas 1998.

regions. In the results section, we discuss the sensitivity to modifications of the sedimentary iron source.

2.4. Ocean Circulation Model and Atmospheric Forcings

[20] The ocean circulation model is a preliminary version of the CCSM 2.0 Parallel Ocean Program (POP) code based on the Los Alamos National Laboratory POP V1.4.3. The model has 100 × 116 horizontal grid points with a resolution of 3.6° longitude and 0.9°–2° latitude (higher near the equator) and a Northern Hemisphere pole rotated into Greenland. There are 25 vertical levels, and the surface layer is 12 m thick, with five levels in the upper 111 m. The model employs the Gent-McWilliams isopycnal mixing parameterization [*Gent and McWilliams*, 1990] and the KPP upper ocean model [*Large et al.*, 1994]. Daily atmospheric forcings are from a 4-year (1985–1989) repeat cycle of NCEP/NCAR reanalysis data [*Large et al.*, 1997; *Doney et al.*, 1998].

2.5. Initial Conditions and Biogeochemical Spin-Up

[21] Zooplankton, DOM, and phytoplankton pools are initialized uniformly at low values. Initial distributions of phosphate, nitrate, and silicate are taken from annual mean values in the World Ocean Atlas 1998 database [*Conkright et al.*, 1998]. Initial values for alkalinity, dissolved oxygen, and dissolved inorganic carbon are from the OCMIP biotic model simulations conducted at NCAR [*Doney et al.*, 2001, 2003]. Following a physical spin-up to approximately steady state, the biogeochemical/ecosystem model control and sensitivity runs are integrated for 24 years, with results presented here from the final year of the simulation. A third-order upwind advection scheme is employed for tracer transport. Small, negative values in surface concentrations arising from advection errors are treated as zero in the biological code and for plotting here.

[22] The lack of a global dissolved iron database is a critical problem facing ocean biogeochemical modeling today [*Johnson et al.*, 2002]. Initially, dissolved iron was set with summer surface values from our mixed layer model (METb) and assigned regional to basin-scale vertical profiles based on sparse published literature values. These depth profiles increased linearly from the surface concentration to 0.6 nM at depth (typically between 400 and 600 m). The deep ocean was set to a uniform initial value of 0.6 nM except for the high-latitude Southern Ocean, where 0.4 nM is applied with a linear transition region from 40°S–50°S. In early simulations, mean iron concentration in the upper 111 m of the water column increased rapidly, roughly doubling during the first decade. This increase was due to lateral spreading of the sedimentary iron source, adjustment to the new scavenging parameterization, and drift in subsurface iron concentrations (in many areas the slope with depth was not linear to 400–600 m). Here we use the iron field from year 12 of a preliminary run as our initial dissolved iron distribution. The drift in mean concentrations in the upper 111 m over the last 4-year forcing cycle was <1% for all nutrients.

3. Results

[23] Similar to our previous findings (METb), the ecosystem model captures to a large degree the observed, large-scale spatial patterns and seasonal cycles in key surface ocean metrics, including nutrient and dissolved iron concentrations (Figures 1 and 2; WOA98, Table 1 of METb,

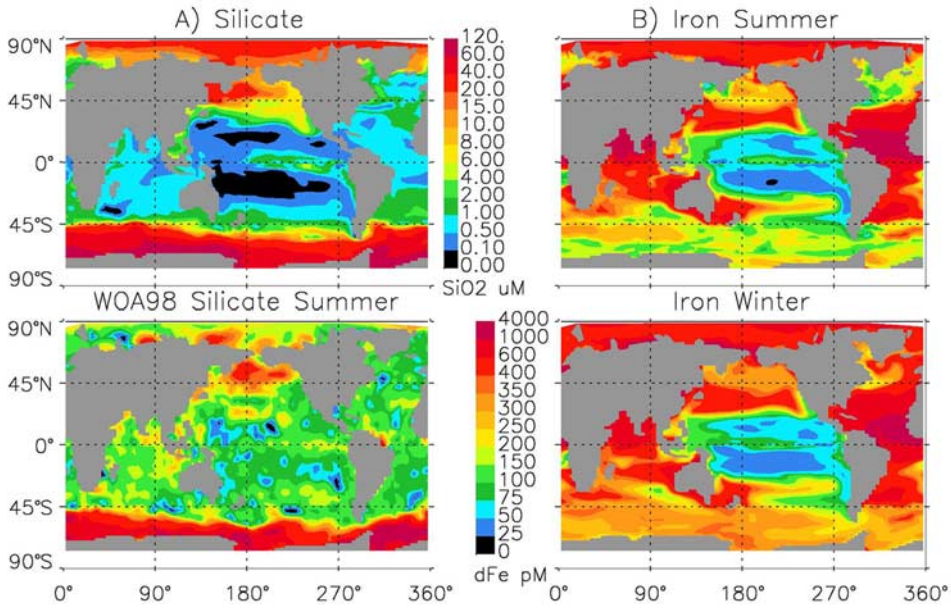

Figure 2. Surface silicate concentrations (summer season in each hemisphere) are compared with climatological concentrations from the World Ocean Atlas 1998. Also shown are the summer and winter season surface dissolved iron concentrations from the model.

and work by *Johnson et al.* [1997] and *de Baar and de Jong* [2001]), surface chlorophyll (Figure 3; SeaWiFS), and primary production (Figure 4; SeaWiFS with VGPM algorithm). Here we highlight key features, differences with the mixed layer model results, and remaining deficiencies. The most significant result is that the inclusion of explicit iron dynamics allows the model to reproduce the HNLC conditions in the Southern Ocean and equatorial and subarctic Pacific Ocean (METa, METb). However, the equatorial Pacific HNLC region is larger in spatial extent

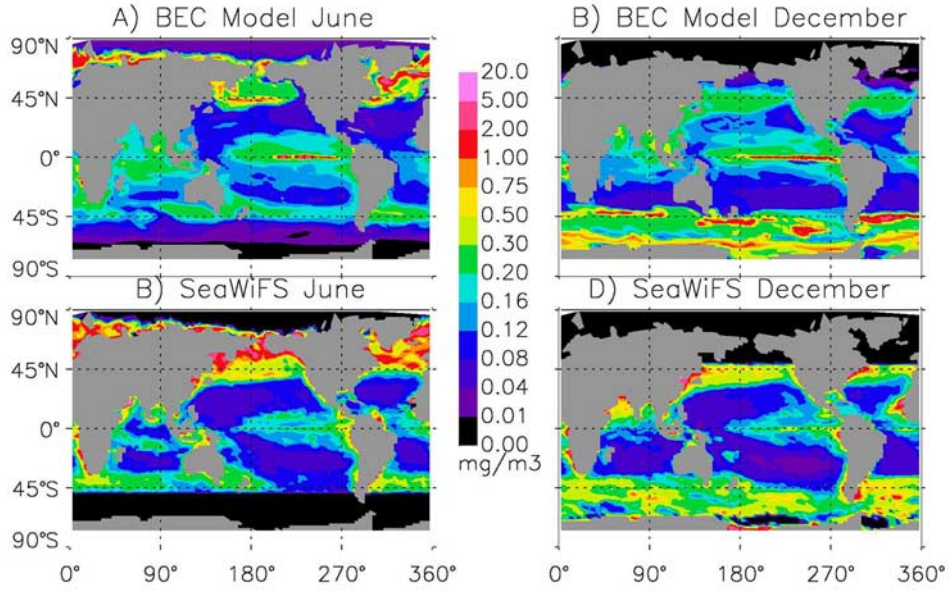

Figure 3. Model surface chlorophyll are compared with SeaWiFS satellite estimates for the months of (a, c) June and (b, d) December.

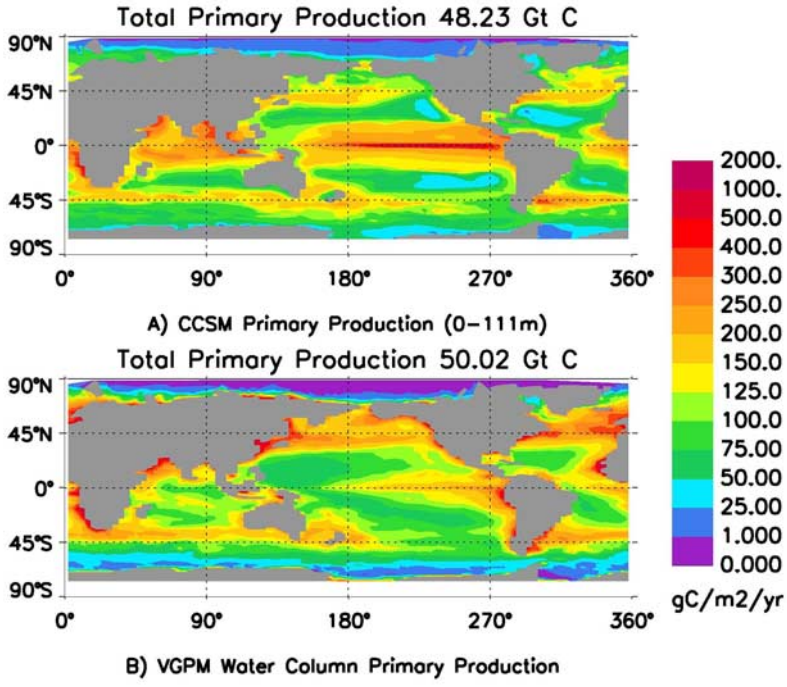

Figure 4. Model simulated annual primary production is compared with a satellite-based productivity estimate using the Vertically Generalized Production Model of *Behrenfeld and Falkowski* [1997] (see *Moore et al.* [2002b] for details of this production estimate).

in the model than in observations, most likely due to excessive upwelling, a common problem with coarse resolution models (see discussion in section 5).

[24] Surface phosphate concentrations are strongly depleted in the North Atlantic gyre due to substantial nitrogen fixation rates early in the simulation. Elsewhere, light and/or iron limitation of nitrogen fixation prevents such strong phosphate depletion. Phosphate concentrations are higher than observations over much of the western Pacific basin where the model has essentially zero surface nitrate, suggesting too little nitrogen fixation and phosphate drawdown. Silicate patterns at basin scale are in broad agreement with the observations but with generally lower surface values (Figure 2). The model does not currently include possibly important silicon sources from dust deposition and riverine runoff. Note the strong Amazon silicate plume in the WOA98 data (Figure 2). Macronutrient concentrations are lower than observations over parts of the subarctic North Pacific but are never fully depleted over the annual cycle.

[25] Model iron concentrations exhibit significant seasonal variability at high latitudes and in the Arabian Sea (Figure 2). In the Southern Ocean, wintertime iron concentrations range from 250 to 350 pM, with a summer drawdown below 150 pM in many areas, in good agreement with recent observations in the SW Pacific [*Measures and Vink*, 2001]. Subarctic North Pacific wintertime iron concentrations are somewhat higher between 300 and 350 pM, reflecting higher atmospheric iron inputs. Iron concentrations are perpetually very low in the equatorial Pacific. High iron concentrations associated with the mineral dust plumes from North Africa and the Arabian Peninsula [*Mahowald et al.*, 2003; *Zender et al.*, 2003] peak during summer season, with large areas exceeding 1.0 nM. Relatively high dissolved iron concentrations also are seen over much of the Arctic Ocean due to the sedimentary iron source and the large shelf areas in this region.

[26] Similar to satellite estimates and METb, model surface chlorophyll concentrations exhibit lowest levels in mid-ocean gyres and at high latitudes during winter, moderate levels (0.2–0.5 mg/m^3) in the HNLC regions, and high levels in the Arctic and North Atlantic in June and in parts of the Southern Ocean in December. Note that chlorophyll concentrations remain well below 1.0 mg/m^3 over most of the Southern Ocean despite high concentrations of the macronutrients (compare with Figures 1 and 2). In general, the model underpredicts chlorophyll concentrations in the eastern boundary current upwelling regions and in coastal waters. The physical processes associated with coastal upwelling are only weakly captured in our coarse resolution ocean model.

[27] Compared with a satellite-based estimate from the Vertically Generalized Production Model (VGPM) [*Behrenfeld and Falkowski*, 1997], model annual mean primary production (Figure 4) is higher in the tropical upwelling zones and over much of the Southern Ocean and lower in the subpolar North Atlantic and North Pacific. *Schlitzer* [2000] suggests that VGPM underestimates production in the Southern Ocean and overestimates production in the North Atlantic based on an inverse modeling

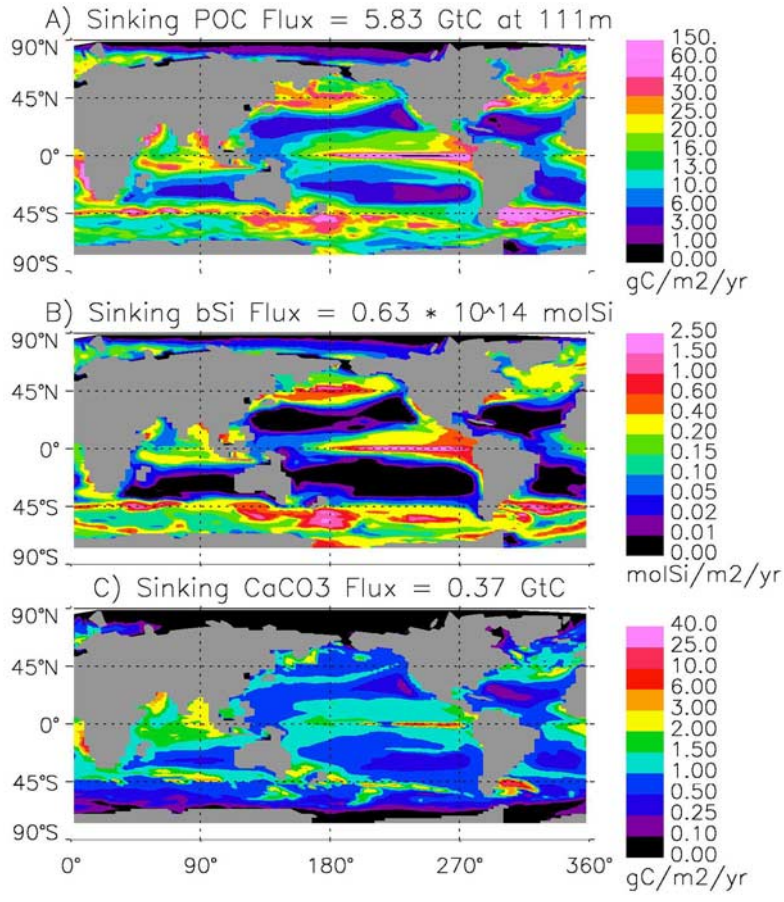

Figure 5. Annual sinking export at 111 m depth of particulate organic carbon, biogenic silica, and calcium carbonate are depicted.

approach. *Buesseler et al.* [2003] also notes that the VGPM underpredicts Southern Ocean productivity relative to field observations along 170°W. The productivity patterns presented here are similar to our previous results (METb), except for the equatorial upwelling regions where production is significantly higher.

4. Export Fluxes

[28] The spatial patterns of annual sinking export of particulate organic carbon (POC), biogenic silica, and calcium carbonate at the base of the euphotic zone (111 m depth) (Figure 5) are similar to those from the mixed layer version (compare with Figures 7 and 12 of METb). The total POC flux, however, is lower at 5.8 GtC at 111 m depth compared with 7.9 GtC at the base of the mixed layer in METb. The coarse resolution GCM is not able to sustain such high export fluxes and is on the low end of model and observational estimates [*Oschlies*, 2001]. Note, however, that export estimates are sensitive to the depth chosen to define the bottom of the net production or euphotic zone as there is a substantial vertical gradient in POC flux with depth (sinking flux is 6.6 GtC at 49 m [see also *Doney et al.*, 2003]). The POC export patterns are driven largely by diatoms (see bSi export) and coccolithophores (see $CaCO_3$ export). Annual export ratios (sinking/PP) range from 0.04 to 08 in the mid-ocean gyres to 0.2–0.38 in mid- to high-latitude bloom regions. *Antia et al.* [2001] estimated annual export ratios (at 125 m) ranging from 0.08 to 0.38 from a large number of sediment trap studies throughout the North Atlantic. Of the dissolved organic carbon (DOC) production of 12.1 GtC, 0.31 GtC is exported from the euphotic zone and remineralized below 111 m (0.49 GtC below 49 m), mainly at high latitudes where there is deep convective mixing in winter.

[29] Most of the model sinking POC pool (global average of 93.4%, at 111 m) is in the easily degraded "free" POC fraction, with remineralization length scales varying between 70 and 643 m (dependent on temperature). The remaining fraction (6.6%) associated with mineral ballast [*Armstrong et al.*, 2002] has much longer remineralization length scales (see Table 2), strongly influencing the POC flux to the deep ocean. The amount of POC associated with each ballast type is a function of the model parameterization, the atmospheric dust deposition, and the $CaCO_3$ and bSi production from the ecosystem model. At 111 m depth, 57.6% of the bound POC is associated with $CaCO_3$, 34.2% with bSi, and 8.2% with sinking dust particles.

This is partially a function of the prescribed higher organic C/ballast ratio for $CaCO_3$ (Table 2). Thus $CaCO_3$ flux dominates transport of organic carbon to the deep ocean in the model. A reasonable range for the calcification/photosynthesis ratio for coccolithophores is 0.2–1.0 [*Robertson et al.*, 1994; *Balch et al.*, 1996]. This range implies coccolithophores in the model account for ~1–4% of primary production. In contrast, diatoms contribute 46% of sinking POC export out of the euphotic zone (including "free" and ballast associated fractions) and 32% of total primary production (compared with 24% in METb). *Aumont et al.* [2003] found that diatoms and their mesozooplankton grazers accounted for 55% of sinking export and 20% of production. *Nelson et al.* [1995] estimated a maximum diatom productivity contribution of 43%, including productive coastal waters.

[30] As in METb, the spatial patterns of $CaCO_3$ production and export are in generally good agreement with the global sediment trap synthesis of *Milliman* [1993] and satellite-based estimates of coccolithophore bloom distributions [*Brown and Yoder*, 1994; *Brown and Podestá*, 1997; *Iglesias-Rodríguez et al.*, 2002]. Highest calcification rates and $CaCO_3$ export are seen over the Patagonian shelf and in some other midlatitude Southern Ocean regions, in the coastal and equatorial upwelling zones, in the Arabian Sea, and in parts of the North Atlantic (Figure 5). The globally integrated calcification is 0.53 GtC, with 0.25 GtC sinking across 1100 m. *Milliman et al.* [1999] estimate global calcification as 0.7 GtC with the flux to the deep ocean (>1000 m) of ~0.3 GtC. Model estimates of deep ocean sinking fluxes at 1100 m for POC and bSi are 0.59 GtC and 41 Tmol Si, respectively.

[31] The model rain ratio (sinking CaCO3/sinking POC) at 111 m integrated globally is 0.065. *Yamanaka and Tajika* [1996] estimate the global rain ratio to be between 0.08 and 0.1. *Sarmiento et al.* [2002] recently argue for a value of ~0.06, with peak values near the equator (>0.08), lower values in the gyres, and minimum values at high latitudes. Their data-model synthesis had a very low rain ratio (0.023) in the North Atlantic, surprising as this region is known for frequent coccolithophore blooms. Our simulated rain ratios over most of the mid- to high-latitude North Atlantic are 0.07–0.12, with a small area exceeding 0.25. We simulate relatively high rain ratios in the gyres (~0.09–0.15) and generally low values at high southern latitudes (<0.05). These patterns in the rain ratio are quite different than the spatial patterns of absolute $CaCO_3$ production. Despite elevated $CaCO_3$ export, the rain ratio in coastal and equatorial upwelling zones is typically low due to high levels of POC export (Figure 5).

[32] Global biogenic silica production in the model is 189 Tmol Si, with about a third (63 Tmol Si) exported across 111 m. The biogenic Si export ratio varies as a function of temperature and the fraction of diatom mortality due to grazing and nongrazing pathways (see section 2 and Appendix A). *Nelson et al.* [1995] estimate a global bSi production of 200–280 Tmol Si/yr and a sinking export of 100–140 Tmol Si based on an assumed export ratio of 50%, and *Gnanadesikan* [1999] computes bSi export at 89 Tmol, arguing that the total is likely $\ll$100 Tmol. *Nelson et al.* [1995] note that at least 50% of bSi dissolves in the upper 100 m of the ocean, with an average dissolution of 58% (export ratio of 0.42) in their observational data sets. Our lower export ratio includes Si released through nongrazing mortality meant to account for viral losses and leakage from cells. In the radiolabeled Si studies cited by *Nelson et al.* [1995], Si that is taken up but then leaks from the cell during the incubation would not be accounted for, possibly reconciling our lower export ratios. *Nelson et al.* [1995] also include coastal diatom production, which is only weakly captured in our GCM.

[33] Regionally, model areal annual bSi production rates qualitatively agree with field estimates. Compared with *Nelson et al.* [1995], model rates are: generally below 0.1 versus 0.2 mol/m^2/yr for the mid-ocean gyres, where diatom production is likely driven by nutrient input from eddies and other mesoscale processes not included in the physical model; 1–2 versus above 8 mol/m^2/yr for underresolved coastal upwelling areas; 0.4–2.0 versus 2.2 mol/m^2/yr for the subarctic Pacific; and 0.3–2.0 versus 0.4–1.0 mol/m^2/yr for the Southern Ocean. Model bSi production rates are higher in the southwest Atlantic sector and the southwest Pacific sector of the Southern Ocean, exceeding 2.0 molSi/m^2/yr. Recent observations during the U.S. JGOFS Southern Ocean study along 170°W found annual production rates of 1.9–3.0 molSi/m^2/yr [*Nelson et al.*, 2001]. *Ragueneau et al.* [2000] summarize available sediment trap data of sinking bSi (mainly from >1000 m) and note a strong latitudinal dependence with low-latitude bSi fluxes typically <0.2 molSi/m^2/yr and fluxes in the mid-ocean gyres <0.03 molSi/m^2/yr. Higher fluxes at these latitudes are seen in coastal upwelling zones and in the equatorial Pacific. Highest sinking fluxes were in the Southern Ocean and the North Pacific, ranging from 0.4 to 0.9 molSi/m^2/yr [*Ragueneau et al.*, 2000] (compare with Figure 5).

4.1. Nitrogen Fixation and Nutrient Limitation Patterns

[34] The spatial pattern of nitrogen fixation in the model is similar to METb (Figure 6), but the total of 55.5 TgN/yr is lower (62.4 TgN in METb) and well below recent observational (80 TgN [*Capone et al.*, 1997]) and geochemical estimates (>100 TgN [*Gruber and Sarmiento*, 1997; *Deutsch et al.*, 2001; *Karl et al.*, 2002]). Such high rates are not sustainable in our coarse resolution GCM; possibly this is because eddies, storms, and other mesoscale processes that are important sources of new nutrients in tropical and subtropical regions are not represented. Also, our sinking export of biogenic material is forced to be a constant molar N/P ratio of 16. However, the N/P ratio of sinking material at HOT is consistently $\gg$16 during times of N fixation [*Christian et al.*, 1997; *Karl et al.*, 2002], and observations in the North Atlantic at BATS show elevated PON/POP and DON/DOP ratios [*Ammerman et al.*, 2003]. Thus, in our model, increasing N fixation tends to deplete phosphate below observed concentrations, causing strong P limitation of the diazotrophs, mainly in the North Atlantic.

[35] As in METb, elevated nitrogen fixation is simulated along the northern coasts of South America and Australia,

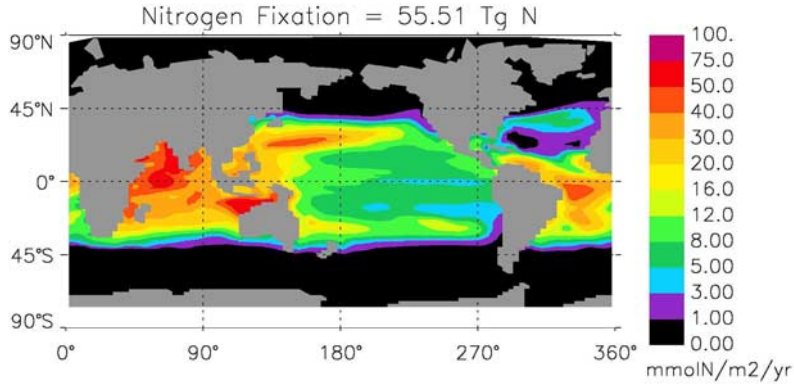

Figure 6. Annual nitrogen fixation rates by the diazotrophs are displayed.

in the Arabian Sea, in the central North Pacific gyre, in the tropical Atlantic, and west of Madagascar. Generally low rates of nitrogen fixation are simulated elsewhere, particularly in the equatorial Pacific, where low dissolved iron concentrations strongly limit diazotroph growth rates. In the North Atlantic, nitrogen fixation rates in the Sargasso Sea are $<\sim 8$ mmolN/m^2/yr (2.4 mmolN/m^2/yr at BATS), well below the rates seen farther south, which are 16–40 mmolN/m^2/yr (Figure 6). The lowest rates in this region (<1 mmolN/m^2/yr) are south of BATS in a region where mixed layers never exceed ~60 m. Thus there is no seasonal entrainment of nutrients from below, and growth of the diazotrophs is strongly P-limited.

[36] Our results in the tropical Atlantic region can be compared with the simulations of *Hood et al.* [2004], which did not include phosphorus as a limiting nutrient. That study predicted substantially higher N-fixation rates in the Gulf of Mexico and in the Caribbean region (~15°N–25°N), more in line with observations than this study. Both simulations show elevated nitrogen fixation along the northern coast of South America and in the eastern North Atlantic adjacent to Africa. *Orcutt et al.* [2001] observed nitrogen fixation rates of ~15 mmolN/m^2/yr at BATS and significantly higher rates farther south. Early in our simulation, N-fixation rates in the BATS region were much closer to the field observations (14.0 mmolN/m^2/yr at year 4). Similarly, rates throughout Caribbean were also higher (20–70 mmolN/m^2/yr, year 4). Thus, phosphate is depleted in the North Atlantic early in the simulation to the extent that simulated nitrogen fixation is too low (particularly north of ~15°N, Figure 6).

[37] Similarly, in the eastern North Pacific at HOT, N fixation is Fe-limited at rates below those observed in situ. Our simulated iron concentrations (~0.11 nM) are at the low end of the observations in this region [*Johnson et al.*, 2003]. The model simulates nitrogen fixation at the HOT site of ~11.5 mmolN/m^2/yr, compared with observational estimates of 31–51 mmolN/m^2/yr [*Karl et al.*, 1997]. Higher N-fixation rates exceeding 40 mmolN/m^2/yr are seen in our simulation in the central North Pacific in the western side of the basin. The general spatial patterns in the Pacific basin including the latitudinal bands of elevated N-fixation and the intensification in the western part of the subtropical gyres are in very good agreement with the N* analysis by *Deutsch et al.* [2001], although total N fixation is lower than their estimate.

[38] In general, the nutrient and light limitation patterns for the three classes of phytoplankton (Figure 7 averaged over summer season in each hemisphere) are similar to those of METb, with several noticeable differences. As already mentioned, the iron-limited area in the equatorial Pacific is larger, and phosphorus-limited areas in the North Atlantic are much more extensive due to modest to high levels of nitrogen fixation early in the simulation, leading to increased phosphate drawdown and export. Recall that subsurface nutrients were held at constant concentrations in METb, so progressive phosphate depletion was not possible despite the generally higher nitrogen fixation rates. In a sensitivity simulation with no N-fixation or primary production by diazotrophs (Table 4 in section 4.3), the P-limited areas for the diatoms and small phytoplankton groups are N-limited instead. Substantial field observations support the idea of strong phosphate depletion and P-limitation of the diazotrophs and perhaps other phytoplankton in the North Atlantic [*Wu et al.*, 2000; *Sañudo-Wilhelmy et al.*, 2001; *Dyhrman et al.*, 2002; *Ammerman et al.*, 2003]. This pattern is consistent with the higher atmospheric iron inputs in the North Atlantic [*Berman-Frank et al.*, 2001].

[39] When nitrogen fixation and diazotroph production are set to zero, primary production declines by 10% from 48.2 GtC in our standard run to 43.3 GtC (Table 4 in section 4.3). Only 0.24 GtC of this difference is due directly to diazotroph production; the remainder is due to increased production by the other phytoplankton groups in response to the new nitrogen introduced by diazotrophs. Even in areas with substantial N-fixation, diazotrophs never account for more than ~5% of annual primary production. The small phytoplankton group benefits preferentially from nitrogen fixation since this group tends to dominate the community in well-stratified areas where diazotrophs thrive. Sinking POC flux at 111 m is 0.47 GtC higher with N-fixation, supporting 8% of global export production in the standard simulation (Table 4 in section 4.3). Direct export from

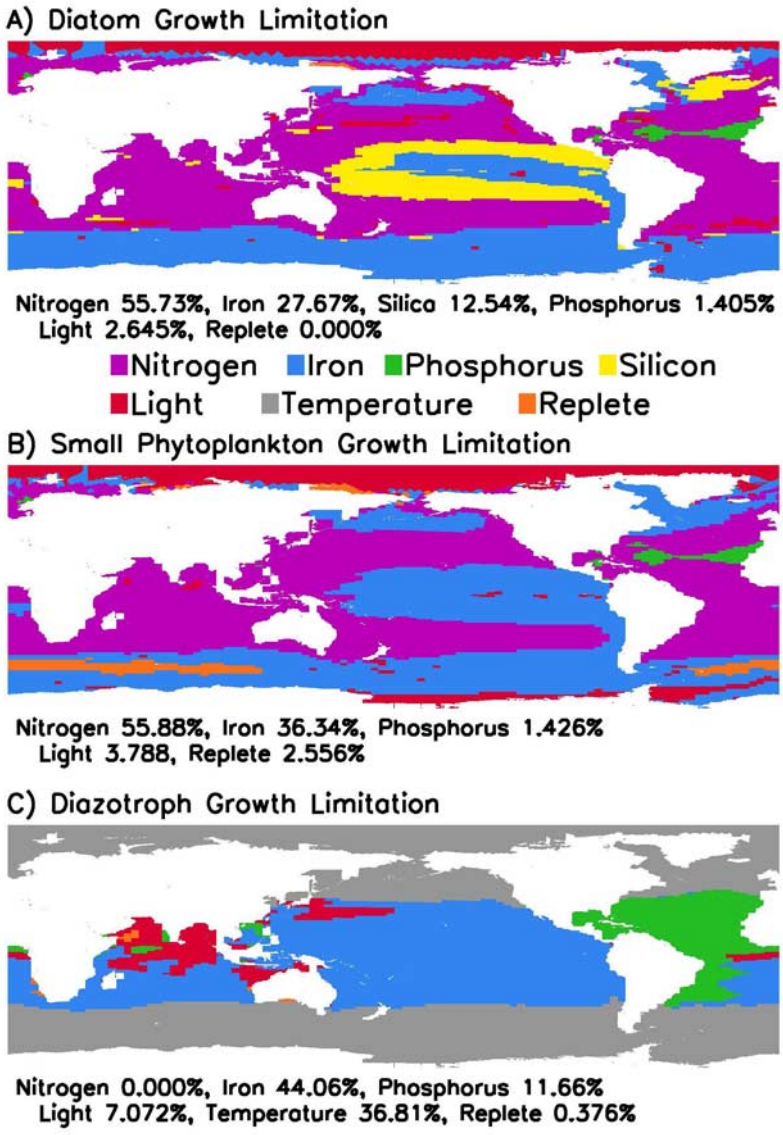

Figure 7. Factor most limiting growth rates is plotted for each phytoplankton group during summer months in each hemisphere.

diazotrophs is negligible in the current model formulation (Appendix A), and this export is mainly due to the diatoms and small phytoplankton. Without N-fixation, there are no areas where phytoplankton growth is P-limited during summer months (compare with Figure 7). Recall that our simulations are on the low end of observational and geochemical estimates of global nitrogen fixation rates. Thus our results should be viewed as minimal estimates of the global impact of nitrogen fixation.

[40] Model phytoplankton can be limited by light, nutrients, and temperature or be "replete." Temperature limitation applies only to the diazotrophs, whose growth rates are drastically reduced at temperatures below 15°C in our model. Light and nutrient limitation are multiplicative (METa), and in Figure 7 we plot the most limiting growth factor in surface waters during summer months. Phytoplankton are termed nutrient and light replete if they are growing at >90% of their maximum temperature-dependent rate. These conditions tend to occur when strong grazing pressure prevents blooms that would otherwise deplete nutrients. This 90% cutoff is an arbitrary definition; using a cutoff of 85% increases the replete area for the small phytoplankton group (mainly in HNLC regions), but has little impact on the diatoms. The diatoms and small phytoplankton are light-limited mainly in high-latitudes areas with heavy sea ice cover and some lower latitude areas due to self-shading within blooms. Owing to their substantially lower initial slope of the production versus irradiance curve, diazotrophs are light-limited over portions of the tropical/subtropical oceans. Most tropical/subtropical areas are iron-limited for the diazotrophs (70% of the areas where temperature is not restricting their growth). The results are consistent with the suggestion by *Berman-Frank et al.* [2001] that for *Trichodesmium* spp., iron is the limiting

nutrient throughout most of the world ocean. However, our results also point to a significant role for the light regime in controlling nitrogen fixation [*Hansell and Feely*, 2000; *Moore et al.*, 2002b; *Hood et al.*, 2004). We can define nutrient-light colimitation as reductions of at least 10% due to the most limiting nutrient, and by at least 10% due to light (phytoplankton growing at $\leq$80% of their maximum rates). By this definition, 20.3% of the ocean is iron-light colimited, and 4.8% if phosphorus-light colimited for the diazotrophs. Smaller areas are iron-light colimited for the small phytoplankton (10.0%) and for the diatoms (4.3%). This definition of colimitation is also arbitrary; if 15% reductions in growth are required, the areas colimited decrease substantially.

[41] The major HNLC regions in the subarctic North Pacific, equatorial Pacific, and Southern Ocean are mainly iron-limited for both diatoms and small phytoplankton. Portions of the Southern Ocean are nutrient-replete (essentially "grazer-limited") for the small phytoplankton when averaged over summer months, but by late summer these areas also tend to be iron-limited. Small phytoplankton are iron-limited over much of the high-latitude North Atlantic, a pattern seen in METb and *Fung et al.* [2000]. Diatoms are Si-limited in the North Atlantic and large portions of the equatorial Pacific. Field observations indicate that Si-limitation terminated the spring diatom bloom during the NABE study [*Sieracki et al.*, 1993]. Most of the Si-limited areas in the Pacific are within our expanded HNLC region and may be partly an artifact of excessive upwelling. In the simulation intense diatom blooms, larger than observed in situ, occur on the equator, depleting Si relative to other macronutrients in the upwelling water. Si growth regulation in this region has been a topic of some debate [*Dugdale and Wilkerson*, 1998; *Dunne et al.*, 1999; *Leynaert et al.*, 2001]. *Aumont et al.* [2003] found no Si-limitation in this region but had similar patterns of Si-limitation in the North Atlantic and more Si limitation in the subantarctic Southern Ocean. Globally, the diatoms and small phytoplankton are iron-limited over 26% and 37% of the world ocean, respectively. *Aumont et al.* [2003] predict that diatom are iron-limited over 40% of the ocean, with much of the difference due to reduced Si-limitation in their simulation. Less of the ocean is iron-limited than in our previous work with the simple physical model (39% for diatoms and 50% for small phytoplankton, METB). Substantial tropical regions in the Indian and Atlantic oceans were iron-limited in that simulation, probably because our fixed subsurface iron concentrations were set too low. The iron-limited areas in the subarctic North Pacific and in the Southern Ocean were also somewhat larger in METB.

4.2. Iron Cycling

[42] Annual dissolved iron uptake by the phytoplankton is 20.7×10^9 mol Fe, similar to the 18×10^9 mol Fe/yr simulated by *Aumont et al.* [2003]. This is surprising given the differences in phytoplankton community composition and Fe/C ratios in the two models. Diazotrophs account for 4.3% of iron uptake, but only 0.5% of primary production, due to their elevated demand for iron (high Fe/C ratios). The global mean Fe/C ratio in our simulation was 5.1 μmol/mol, with considerable regional variations. This is quite similar to the mean value of 5 μmol/mol suggested by *Johnson et al.* [1997] and the value of 5.1 μmol/mol simulated by *Aumont et al.* [2003]. Mean Fe/C in sinking export at 111 m was 5.5 μmol/mol higher due to scavenged iron.

[43] The sedimentary and atmospheric sources for dissolved iron are similar in magnitude (Figure 8) but with very different spatial distributions. The sedimentary source is localized in the few shallow regions, while most of the atmospheric deposition (77%) occurs near desert sources (within 14% of total ocean area), with a more diffuse atmospheric deposition spread globally. Comparing the sedimentary iron source with the scavenging loss to the sediments (Figure 8), it is apparent that much of the iron released from the sediments is removed locally by scavenging. Similarly, in areas with high dust deposition, much of the iron input is removed by scavenging. Iron concentrations exceed 0.6 nM in these areas, and model scavenging rates increase rapidly above this level.

[44] Global budget terms for the iron cycle, including sediment and atmosphere inputs, sediment deposition, and upper ocean residence times, are summarized in Table 3. Residence times are calculated as total dissolved iron divided by sinking particulate iron export. This ignores mixing/subduction export of dissolved inorganic and organic iron, which is likely a small loss at 466 m but may be significant at 111 m. Areas of sedimentary input or high dust deposition have high scavenging rates and generally short residence times. In Table 3, we divide the ocean into areas of high iron inputs (sedimentary source and/or dust deposition >1.6 g dust/m^2/yr, 18.2% of total ocean area) and remaining areas with low external inputs of dissolved iron (81.8% of ocean area). Residence times are longer in the areas with low inputs, where dissolved iron concentrations are typically well below 0.6 nM. Mean residence times of 1–4 months for surface waters (to 100 m) and 15–41 years for the deep ocean were estimated by *de Baar and de Jong* [2001].

[45] *Aumont et al.* [2003] and *Gregg et al.* [2003] make different assumptions about the iron content of dust, prescribe a surface solubility of 1%, and do not allow for subsurface dust dissolution and iron release. In our model, subsurface dust dissolution releases an additional 2.2×10^9 mol Fe/yr of bioavailable iron in the upper 111 m. Our bioavailable iron input from dust deposition to the upper 111 m (including surface and subsurface dissolution) is 8.1×10^9 mol Fe/yr with an additional 2.5×10^9 mol Fe/yr from the sediments (Table 3). As these models have similar biological uptake rates and maintain reasonable surface dissolved iron concentrations, the losses to scavenging must be substantially higher in our simulation. Previously, we estimated an input of 5.3×10^9 mol Fe/yr using the same dust deposition [*Tegen and Fung*, 1995] as *Aumont et al.* [2003] but with 2% surface solubility and different assumptions about iron content in the dust (METb). *Fung et al.* [2000] estimated surface inputs of $1-10 \times 10^9$ mol Fe/yr assuming a surface solubility of 1–10%. These differences highlight the large uncertainties surrounding iron inputs and

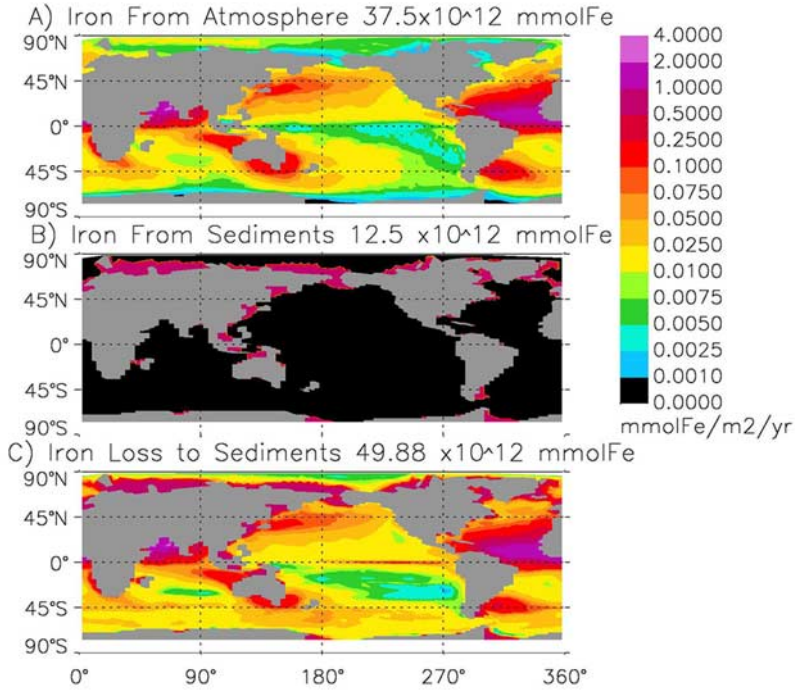

Figure 8. Displayed are the dissolved iron inputs integrated over the total water column (a) from the sediments and (b) from atmospheric dust deposition. (c) Also shown is the iron loss to ocean sediments due to scavenging.

Table 3. Global Sinks and Source of Dissolved Iron in the World Ocean[a]

Sink or Source	Value[b]	Mean Concentration
Input from dust deposition (surface)	5.84	
Input from dust deposition (<111 m)	8.06	
Input from dust deposition (<466 m)	13.7	
Input from dust deposition (total)	37.5	
Sedimentary input (<111 m)	2.51	
Sedimentary input (<466 m)	7.59	
Sedimentary input (total)	12.5	
Total inputs	50.0	
Total scavenging loss to sediments	49.9	
Total dissolved iron (<111 m)	15.1	0.38 nM
Total dissolved iron (<466 m)	76.1	0.47 nM
Mean residence time (<111 m)	1.3 years	
Mean residence time (<466 m)	3.5 years	
High Iron Input Regions (18.2% of Total Ocean Area)		
Total dissolved iron (<111 m)	5.2	0.73 nM
Total dissolved iron (<466 m)	19.2	0.68 nM
Residence time (<111 m)	0.61 years	
Residence time (<466 m)	1.1 years	
Low Iron Input Regions (81.8% of Total Ocean Area)		
Total dissolved iron (<111 m)	9.9	0.31 nM
Total dissolved iron (<466 m)	56.9	0.42 nM
Residence time (<111 m)	3.7 years	
Residence time (<466 m)	14.4 years	

[a]High iron input areas are defined as areas with sedimentary input and/or atmospheric dust deposition >1.6 gDust/m^2/year.
[b]Residence times are estimated by dividing the total dissolved iron pool during December by the annual sinking particulate iron flux. Residence times are estimated for the global ocean and for high and low iron input regions separately. Units are $\times 10^{12}$ mmol Fe/yr, unless noted otherwise.

Table 4. Sensitivity of Marine Ecosystem and Biogeochemical Cycling to Variations in N-Fixation and Iron Inputs[a]

	PP	Sink	Nfix	%Diat	%Sp	%Diaz	dFe	Tres	DiatPP%
Standard	48.2	5.84	55.5	27.7	36.3	44.1	0.38	1.3	31.6
NoSedFe	48.1	5.80	55.0	27.9	37.7	44.5	0.37	1.7	31.3
NoNfix	43.3	5.37	0.0	27.5	34.6	–	0.40	1.4	33.5
Zend03	46.7	5.38	46.9	32.8	45.8	49.6	0.30	1.4	29.6
Dustx0.1	40.9	4.21	27.2	57.2	70.8	54.9	0.18	1.6	26.1
Dustx0.25	44.0	4.74	34.6	44.4	59.9	52.2	0.23	1.6	27.0
Dustx0.5	46.6	5.27	43.8	35.6	49.5	49.7	0.29	1.5	28.2
Dustx2	49.3	6.44	67.6	20.2	24.6	35.5	0.50	1.0	34.5
Dustx4	49.7	6.91	78.3	14.6	15.4	26.5	0.61	0.69	36.2
Dustx10	49.9	7.36	85.6	9.37	7.66	14.1	0.79	0.38	38.4

[a]Results shown are from year 24. PP, primary production (Gt C); Sink, sinking particulate organic carbon flux at 111m (Gt C); Nfix, global nitrogen fixation (Tg N); %Diat, %Sp, %Diaz, percentage of ocean area iron-limited (summer months); dFe, global mean iron concentration in the upper 111 m of the ocean (nM); Tres, global mean residence time for iron in upper 111 m (years); DiatPP%, percentage of total productivity by diatoms. Runs include NoNfix, with no nitrogen fixation; NoSedFe, no sedimentary iron source; Zend03, with dust input from the climatology of *Zender et al.* [2003]; Dustx0.1, Dustx0.25, and Dustx0.5, dust flux reduced by factors of 0.1, 0.25, and 0.5; Dustx2, Dustx4, and Dustx10, dust flux increased by factors of 2, 4, and 10.

questions of solubility, bioavailability, and scavenging losses.

4.3. Sensitivity to Variations in Iron Inputs

[46] Reducing the magnitude of the sedimentary iron source to zero has modest effects on global scale primary production, export production, nitrogen fixation, and areal extent of iron limitation (Table 4). The BEC model is relatively insensitive to this modification because most of the sediment iron input is lost rapidly via scavenging within a relatively small area. Mean iron concentration in the bottom cell in shallow regions declines from ~1.7 nM in our standard run to 0.52 nM with no sediment source. Areas iron-limited for all phytoplankton groups increase by at most a few percent globally, mostly in the Arctic Ocean. Nearly the entire Arctic becomes iron-limited for diatoms and iron- or light-limited for the small phytoplankton without the sedimentary source, in contrast to our standard run where the shelf regions are mainly N-limited (Figure 7). Atmospheric iron inputs are generally low at these high northern latitudes.

[47] Variations in atmospheric iron inputs, in contrast, have significant global impacts (Table 4). The responses are similar in magnitude to those found in METb for short-term (<3 years) experiments with fixed, subsurface nutrient concentrations. We examine the sensitivity of forcing the model with the climatological dust flux from *Zender et al.* [2003], and we compare our standard run with multidecadal simulations where the standard dust flux is multiplied by factors of 0.1, 0.25, 0.5, 2, 4, and 10, likely bounding the possible variations in dust deposition to the oceans due to climate variations. *Mahowald et al.* [1999] estimate that global dust loading to the atmosphere was 2.5 times higher at the Last Glacial Maximum (LGM), with twenty-fold increases seen at high latitudes. This resulted in a 4.6-fold increase in dust deposition to the oceans (METb). *Mahowald and Luo* [2003] estimate that dust fluxes could decline by 60% by 2100.

[48] When dust flux is doubled (Dustx2), primary production increases by 1.1 GtC, sinking POC export by 0.6 GtC, and nitrogen fixation by nearly 22% to 68 TgN/yr (Table 4). Note that these differences are the sustained decadal timescale response to variation in iron inputs (24-year runs). Much of the enhanced nitrogen fixation is in the western Pacific basin, the spatial pattern similar to *Deutsch et al.* [2001]. N-fixation at HOT grows from 11.5 to 23.3 mmolN/m^2/yr. The HNLC regions shrink, nearly disappearing in the subarctic North Pacific, where macronutrients are seasonally depleted (N limitation), and the size of the equatorial Pacific HNLC region is significantly smaller. Increasing dust flux fourfold (Dustx4) leads to even larger ecological responses, with the equatorial Pacific HNLC region shrinking smaller than observed and the entire subarctic North Pacific switching to N-limitation during summer months. In the extreme case of a tenfold increase in dust flux (Dustx10), export production increases over the standard simulation by 1.5 GtC/yr, nitrogen fixation increases to 86 TgN/yr, and only small portions of the equatorial Pacific remain iron-limited, but notably most of the high-latitude Southern Ocean is still iron-limited during summer months (though with large increases in POC export). Decreasing dust flux has similar impacts, reducing global export fluxes and nitrogen fixation significantly (Table 4). The area iron-limited for each phytoplankton group during summer months also varies directly with dust inputs from the atmosphere, increasing to ~50% of the world ocean for the diazotroph and small phytoplankton groups when dust is reduced by half (Table 4). The dust climatology of *Zender et al.* [2003] results in reductions in primary and export production, nitrogen fixation, and mean surface iron concentrations relative to our standard run. These results are consistent with a lower total oceanic dust deposition in this climatology relative to the standard simulation [from *Luo et al.*, 2003].

[49] Higher atmospheric iron inputs tend to favor diatom production in HNLC regions (as in METb). Diatoms account for 31.6% of global primary production in our standard run, increasing to 34.5% in the ×2 simulation. In general, the contribution of diatoms to primary production scales directly with dust inputs, increasing at higher iron inputs and decreasing at lower dust fluxes (Table 4). As iron increases, diatoms have an advantage due to their lower grazing losses, while at lower iron concentrations the diatoms are not as efficient at iron uptake. Mean upper ocean iron concentrations also scale proportional to dust inputs, and the mean residence time varies inversely with dust deposition (Table 4). The residence time is partly a function of the iron scavenging parameterization, where

scavenging rates are scaled with iron concentration (see Appendix A). Scavenging rates increase sharply at high iron concentrations, resulting in decreased residence time in surface waters. We note that similar processes must be at work in the real ocean to maintain the relatively narrow range of observed iron concentrations (~fourfold variation [*Johnson et al.*, 1997]) given atmospheric inputs that vary by several orders of magnitude.

[50] In a sensitivity experiment with ×10 atmospheric iron input, *Aumont et al.* [2003] found initial strong increases in primary and export production, while on longer timescales, primary production decreases while export production remains elevated (increased by ~1.2 GtC/yr for several hundred years). Export production in our Dustx10 experiment is elevated by 1.5 GtC/yr after 24 years relative to our standard run (Table 4). *Aumont et al.* [2003] had a very similar increase in export after 24 years (~1.6 GtC/yr, their Figure 11). Our model maintains elevated primary and export production partly due to the inclusion of the diazotrophs, where increasing iron inputs increase N-fixation and primary production in the tropics and subtropics. Shifting phytoplankton community composition toward diatom dominance also does not increase export ratios as strongly in our model as in the work of *Aumont et al.* [2003].

[51] The responses seen in nitrogen fixation, export, and primary production to variations in atmospheric iron inputs to the oceans are nonlinear (Table 4). Primary production is relatively unaffected, except for the Dustx0.1 and Dustx0.25 simulations, where there is a strong decline. Larger responses to dust variations are seen in export production (Table 4). This is because changes in ecosystem dynamics and community composition in response to changing iron inputs alter the export ratio in such a way as to minimize changes to total primary production in the model. Increasing iron fluxes to the HNLC regions shift the community composition from picoplankton dominance to increasing diatom production (Table 4) and to increasing contributions from coccolithophores (as the small phytoplankton biomass increases). Both of these community shifts increase the material from primary production routed to sinking particulate export (see section 2 and Appendix A). Similarly, as dust fluxes are reduced, the community is increasingly shifted toward low-biomass, picoplankton-dominated communities with lower export ratios.

[52] It should be noted that multiplying global dust fluxes by constant factors is a somewhat crude modification. In reality, dust deposition changes with climate, when wind-forcing and dust source regions are modified. In our simulation, when dust fluxes are doubled, most of the increase comes in areas with already heavy dust deposition (see Table 3). Thus most of the additional iron is lost to scavenging. Only the iron added to regions where iron is the growth-limiting nutrient directly impacts primary and export production. For the diatoms and small phytoplankton, this is mainly in the classic HNLC regions. For the diazotrophs, iron is the limiting nutrient over most tropical/subtropical regions. This is why nitrogen fixation rates respond in such a strong way to iron input variations (Table 4). Increasing nitrogen fixation then fuels additional primary and export production by the diatoms and the small phytoplankton, which tend to be nitrogen-limited in these regions. At the HOT site near Hawaii, increasing dust inputs by factors of 2 and 4 increases annual nitrogen fixation rates by factors of 2 and 3, respectively. At higher dust inputs (Dustx10), light limitation and grazing pressure prevent further large increases in nitrogen fixation at HOT. Changes in dust source regions that increase dust flux by larger factors, specifically in the high-latitude HNLC regions, could result in larger changes to global export than seen here. This has been suggested for the Last Glacial Maximum where expansion of dust source regions led to greater than twenty-fold increases in dust deposition to parts of the Southern Ocean [*Mahowald et al.*, 1999].

[53] In any given year, most of the iron supporting phytoplankton uptake (~70–80%) comes from below through entrainment and mixing of subsurface iron [*Archer and Johnson*, 2000; *Moore et al.*, 2002b; *Aumont et al.*, 2003] (also this study). Owing to the relatively short residence times for iron, however, subsurface iron concentrations are ultimately dependent on atmospheric deposition. Without continual surface input, iron would be rapidly depleted in the upper water column by biology and adsorption to and removal by sinking particles. In the simulations where dust flux was altered, listed in Table 4, export production and nitrogen fixation rates respond quickly, within a couple of years, and then maintain at either elevated or depressed levels relative to the standard simulation for 2 decades. The timescale for ocean biogeochemistry to respond to changes in dust deposition is short because of the short residence time for iron in the upper ocean (Tables 3 and 4). Significant interannual and decadal timescale variability in dust deposition to the oceans [*Mahowald et al.*, 2002, 2003] should, therefore, modulate upper ocean biogeochemistry and air-sea CO_2 flux over these timescales.

5. Summary and Discussion

[54] The coupled BEC model qualitatively, and to a large degree quantitatively, reproduces observed global-scale patterns of surface nutrient concentrations, primary production, and sinking export of particulate organic carbon, biogenic silica, and calcium carbonate. The model captures the known ecological contributions of key phytoplankton functional groups, including diatoms, coccolithophores, and diazotrophs. Diatoms dominate the flux of POC out of surface waters (46%), while accounting for 32% of total primary production. The mineral ballast model as implemented gives a larger role to the coccolithophores in terms of POC flux to the deep ocean (>1000 m). Nitrogen fixers account for a small fraction of primary production, but indirectly fuel 10% of primary production and 8% of sinking POC export out of surface waters. Our model underestimates total N-fixation relative to recent observationally based estimates by a factor of 2 or more, and thus these impacts on primary and export production are also likely low.

[55] One deficiency in the simulation is the enlarged size of the equatorial Pacific HNLC region compared with

observations. Similar problems are apparent in previous global simulations [*Palmer and Totterdell*, 2001; *Bopp et al.*, 2001; *Aumont et al.*, 2003]. The cold tongue associated with upwelling in our simulation is often larger and extends farther west than seen in satellite observations. Thus it is likely that the enlarged HNLC is driven by excessive equatorial upwelling, a common problem in coarse resolution circulation models [*Gnanadesikan et al.*, 2002]. Subsurface nutrient concentrations along the equator generally agree with observations, suggesting that nutrient trapping [*Oschlies*, 2000] is not the major issue. Doubling dust deposition reduces the size of HNLC region, but the dust deposition in the standard run compares favorably with measurements on Oahu and Midway islands (even somewhat higher than observations [*Luo et al.*, 2003]). We cannot rule out the possibility that the iron solubility at deposition may be too low [see *Johnson et al.*, 2003]. Significantly, increased dust flux or surface solubility is inconsistent with iron limitation in the subarctic North Pacific in the model. However, we assume a constant solubility, and there are likely spatial and temporal variations in solubility that may also play a role in our large equatorial HNLC region.

[56] Simulated productivity, community structure, and carbon export all exhibit considerable sensitivity, sustainable over decadal timescales, to shifts in atmospheric dust deposition. While broadly supporting the Martin hypothesis that large increases in dust deposition during ice age periods led to enhanced biological export of carbon to the deep ocean [*Martin*, 1990; *Martin et al.*, 1991; *Moore et al.*, 2000], some caution is necessary, as our simulations represent a much shorter timescale than the ocean biogeochemical response over glacial-interglacial periods. In future work, we plan to quantify how decadal to century timescale variations in dust deposition influence ocean biogeochemistry and air-sea CO_2 exchange. Global-scale nitrogen fixation is also sensitive to variation in atmospheric iron inputs, supporting the findings of *Berman-Frank et al.* [2001] that iron likely limits N-fixation rates over much of the tropics and subtropics. However, our results also point to a significant role for mixed layer depth and the associated light regime in controlling nitrogen fixation [*Hansell and Feely*, 2000; *Moore et al.*, 2002b; *Hood et al.*, 2004] (also this study). Over the coming century these warm water regions are predicted to become more stratified as a result of global warming [*Sarmiento et al.*, 2004], potentially leading to enhanced nitrogen fixation in many regions [*Boyd and Doney*, 2002] as has been observed at the HOT site during periods of increased stratification [*Karl et al.*, 1995]. However, reduced dust deposition [*Mahowald and Luo*, 2003] could act to offset this potential increase in nitrogen fixation.

[57] The BEC model is considerably less responsive to variations in the sedimentary iron source. This is because significant portions of the atmospheric input go to open ocean, iron-limited regions, while the sedimentary source is more localized. The sedimentary source is critical in the Arctic Ocean and portions of the high-latitude North Atlantic, and likely accounts for much of the difference in phytoplankton bloom dynamics in the northern versus southern high-latitude regions. Around much of Antarctica the continental shelf is narrow and steep. The few areas with larger shelf regions are notably the areas where phytoplankton blooms are observed most frequently [i.e., *Moore and Abbott*, 2000].

[58] The results presented here are encouraging that sufficient ecological complexity can be captured at the global-scale to use coupled models to predict the ecological and biogeochemical response of the oceans to changing climate conditions. Future work will examine the links and feedbacks between dust deposition, climate, marine ecosystem dynamics, and ocean biogeochemistry.

Appendix A

A1. Iron Scavenging

[59] The iron scavenging rate (1/yr) is parameterized based on ambient iron concentration and the number of particles available to scavenge iron:

$$\begin{aligned}
\text{Fe_scav} &= 0.12\times \\
&\quad \text{MIN}((\text{sinking dust} + \text{sinking POC} + \text{all other POC}) \\
&\quad /\text{Ref_Particle}), 4.0), \\
\text{Fe_scav} &= \text{Fe_scav} \times (\text{dFe}/0.4) \qquad \text{for dFe} < 0.4 \text{ nM}, \\
\text{Fe_scav} &= \text{Fe_scav} \\
&\quad + ((\text{dFe} - 0.6) \times (6.0/1.4)) \qquad \text{for dFe} > 0.6 \text{ nM}.
\end{aligned}$$

[60] A base scavenging rate of 12%/yr is reduced in areas where standing particle concentration plus the sinking particle flux falls below a threshold value. The reference value (Ref_Particle = 0.0066 nmolC/cm^2/s) is set relatively high such that the base scavenging rate is reduced in most regions, particularly at depth. Dust and standing POC are scaled to give similar units to sinking POC flux. Standing stock of POC (nmolC/cm^3) is scaled by a factor of 0.002, and sinking dust (gDust/cm^2/s) is scaled by a factor of 8.33e7. This gives an approximately equal scavenging weight to dust and POC. We are unaware of any studies accessing the relative scavenging efficiency of dust and organic particles, an area in need of further research.

[61] The scavenging rate is also influenced by ambient dissolved iron concentrations, reduced at iron concentrations below 0.4 nM, and increased sharply above 0.6 nM. At low concentrations, nearly all dissolved iron is bound to strongly binding ligands and is only weakly particle reactive. At higher iron concentrations an increasing portion of the dFe is bound to weaker ligands or exists as free ions (and will be much more particle reactive). At very high iron concentrations, dissolved iron will eventually precipitate to form iron oxides. Most modeling studies have assumed that scavenged iron is permanently lost from the system [*Archer and Johnson*, 2000; *Moore et al.*, 2002a; *Christian et al.*, 2002]. However, this is unlikely to be the case since many of the particles themselves will dissolve/remineralize at some depth in the oceans, and first principles would suggest a reversible process. We put 10% of the scavenged iron onto our sinking detritus and allow it to remineralize deeper in the water column. The remaining 90% is assumed lost to the sediments.

A2. Routing of Organic Materials Upon Mortality

[62] The routing of biomass between particulate, dissolved, and inorganic pools varies by type of phytoplankton

and type of mortality. In general, the portion of the organic matter not routed to sinking POM is split between the semilabile DOM pools (30%) and remineralization (70%). Remineralization is meant to account for direct remineralization and for material released as labile DOM which would rapidly remineralize. Aggregation losses are routed to the sinking POM pools (100%). The daily nongrazing mortality/respiration loss term is routed 5% to the sinking POM pools for the diatoms, and a small percentage based on the $CaCO_3$ present is routed to sinking pools for the small phytoplankton group. None of the diazotroph nongrazing mortality is routed to sinking detritus. For all three groups, the fraction not routed to sinking POM is split between remineralization (70%) and semilabile DOM (30%).

[63] When diatoms are grazed, 30% of grazed organic matter goes to new zooplankton biomass [*Straile*, 1997], 26% is routed to POM, 13% is routed to semilabile DOM, and 31% is remineralized. When diazotrophs are grazed, 21% of the organic matter is routed to new zooplankton biomass, 0% is routed to sinking detritus as their grazers typically do not form sinking fecal pellets, and 24% is routed to DOM and 55% is routed to remineralization based on work by *O'Neil* [1999] and *O'Neil et al.* [2004]). The diazotrophs have high C/N/P relative to the Redfield values; when they are grazed, sufficient C and N are routed to the zooplankton pool and to the sinking POM pool to achieve Redfield values relative to the grazed P. The remainder is split between remineralization (70%) and DOM (30%).

[64] When the small phytoplankton are grazed, 30% of the organic material is routed to new zooplankton biomass [*Straile*, 1997] and 36% is remineralized. The remainder is split between the sinking and DOM detrital pools with a function that varies based on $CaCO_3$ and C biomass levels. Enough organic carbon must be routed to the sinking pool to fulfill the mineral ballast requirements for $CaCO_3$. Thus, as calcification increases, the portion of organic matter routed to the sinking pool must increase. We also modify the portion routed to the sinking pool as a function of biomass. This is an attempt to capture the ecosystem dynamics associated with cell size. When biomass levels are low, the assemblage is typically dominated by very small picoplankton with single celled grazers that do not produce fecal pellets, thus producing little sinking export. As biomass increases, particularly under bloom conditions, larger sized cells become more important components of the assemblage, and thus we route an increasing proportion of organic matter to the sinking pool up to a maximum of 24%. At low biomass levels seen in the mid-ocean gyres, approximately 6% is routed to sinking POM.

[65] Zooplankton mortality is also routed among particulate and dissolved detrital pools based on the current prey being consumed (METa). A fraction of zooplankton mortality is routed to the sinking particulate pool (fraction to POC = (13.3% of diatom grazing rate + 6.66% of grazing on small phytoplankton + 3.33% of grazing on diazotrophs)/by the total grazing rate on all phytoplankton groups). This is a much lower fraction than in METa. The remaining material is split between DOM (30%) and remineralization (70%). Note that for the diatoms, 26% of the grazed material is routed directly to sinking detritus and an additional ~4% (0.3×0.133) is routed to sinking detritus after passing through the zooplankton pool (30% total). For small phytoplankton, the maximum export ratio is 26% from these pathways. Approximately 0.7% of grazed diazotroph material goes to sinking detritus (0.21×0.033).

[66] Grazing also influences the routing of bSi and $CaCO_3$. Diatom nongrazing mortality (which represents excretion of nutrients, cell lysis, respiration losses, etc.; see METa) leads to a high remineralization in the upper water column (95% of the silicon enters the dissolved silicate pool). This remineralization is aided by bacterial degradation of organic coatings [*Bidle and Azam*, 1999], a process not explicit in the model. Half of the grazed Si is remineralized, due to direct remineralization in the zooplankton gut and due to the removal of organic coatings leading to a rapid remineralization. All of the bSi enters the sinking detrital pool from aggregation losses. Previously, we assumed that 50% of grazed CaCO3 was remineralized (METa). *Jansen and Wolf-Gladrow* [2001] suggest that this percentage is too high. Here we set remineralization to one third of the grazed $CaCO_3$, accounting for some re-ingestion of fecal material in the upper water column [*Jansen and Wolf-Gladrow*, 2001], a process not included explicitly in the model.

[67] **Acknowledgments.** The authors wish to thank John Dunne for helpful comments and insights on this paper. The authors thank the Climate Simulation Laboratory at the National Center for Atmospheric Research for time on the NCAR computers. We also thank the SeaWiFS project (code 970.2) and the Distributed Active Archive Center (code 902) at the Goddard Space Flight Center, Greenbelt, Maryland, for the production and distribution of the ocean color data, respectively. This work was funded by NSF grant OCE-0222033 and the National Center for Atmospheric Research. This is JGOFS contribution 11076 and WHOI contribution 11210.

References

Ammerman, J. W., R. R. Hood, D. A. Case, and J. B. Cotner (2003), Phosphorus deficiency in the Atlantic: An emerging paradigm in oceanography, *Eos Trans. AGU*, *84*(18), 165.

Anderson, L. A., and J. L. Sarmiento (1994), Redfield ratios of remineralization determined by nutrient data analysis, *Global Biogeochem. Cycles*, *8*, 65–80.

Antia, A. N., et al. (2001), Basin-wide particulate carbon flux in the Atlantic Ocean: Regional export patterns and potential for atmospheric CO_2 sequestration, *Global Biogeochem. Cycles*, *15*, 845–862.

Archer, D. E., and K. Johnson (2000), A model of the iron cycle in the ocean, *Global Biogeochem. Cycles*, *14*, 269–279.

Armstrong, R. A., C. Lee, J. I. Hedges, S. Honjo, and S. G. Wakeham (2002), A new, mechanistic model for organic carbon fluxes in the ocean based on the quantitative association of POC with ballast minerals, *Deep Sea Res., Part II*, *49*, 219–236.

Aumont, O., E. Maier-Reimer, S. Blain, and P. Monfray (2003), An ecosystem model of the global ocean including Fe, Si, P co-limitations, *Global Biogeochem. Cycles*, *17*, 1060, doi:10.1029/2001GB001745.

Balch, W. M., J. Fritz, and E. Fernandez (1996), Decoupling of calcification and photosynthesis in the coccolithophore *Emiliana huxleyi* under steady-state light-limited growth, *Mar. Ecol. Prog. Ser.*, *142*, 87–97.

Barbeau, K., J. W. Moffett, D. A. Caron, P. L. Croot, and D. L. Erdner (1996), Role of protozoan grazing in relieving iron limitation of phytoplankton, *Nature*, *380*, 61–64.

Behrenfeld, M. J., and P. Falkowski (1997), Photosynthetic rates derived from satellite-based chlorophyll concentration, *Limnol. Oceanogr.*, *42*, 1–20.

Berman-Frank, I., J. T. Cullen, Y. Shaked, R. M. Sherrell, and P. G. Falkowski (2001), Iron availability, cellular iron quotas, and nitrogen fixation in *Trichodesmium*, *Limnol. Oceanogr.*, *46*, 1249–1260.

Bidle, K. D., and F. Azam (1999), Accelerated dissolution of diatom silica by marine bacterial assemblages, *Nature*, *397*, 508–512.

Blackmon, M. B., et al. (2001), The Community Climate System Model, *Bull. Am. Meteorol. Soc.*, *82*, 2357–2376.

Bopp, L., P. Monfray, O. Aumont, J. L. Dufresne, H. Le Treut, G. Madec, L. Terray, and J. C. Orr (2001), Potential impact of climate change on marine export production, *Global Biogeochem. Cycles*, *15*, 81–99.

Boyd, P. W., and S. C. Doney (2002), Modeling regional responses by marine pelagic ecosystems to global climate change, *Geophys. Res. Lett.*, *29*(16), 1806, doi:10.1029/2001GL014130.

Boyd, P. W., and P. J. Harrison (1999), Phytoplankton dynamics in the NE subarctic Pacific, *Deep Sea Res., Part II*, *46*, 2405–2432.

Brown, C. W., and G. P. Podestá (1997), Remote sensing of coccolithophore blooms in the western South Atlantic Ocean, *Remote Sens. Environ.*, *60*, 83–91.

Brown, C. W., and J. A. Yoder (1994), Coccolithophorid blooms in the global ocean, *J. Geophys. Res.*, *99*, 7467–7482.

Brzezinski, M. A. (1985), The Si:C:N ratio of marine diatoms: Interspecific variability and the effect of some environmental variables, *J. Phycol.*, *21*, 347–357.

Buesseler, K. O. (1998), The de-coupling of production and particulate export in the surface ocean, *Global Biogeochem. Cycles*, *12*, 297–310.

Buesseler, K. O., R. T. Barber, M. L. Dickson, M. R. Hiscock, J. K. Moore, and R. Sambrotto (2003), The effect of marginal ice-edge dynamics on production and export in the Southern Ocean along 170°W, *Deep Sea Res., Part II*, *50*, 579–603.

Capone, D. G., J. P. Zehr, H. W. Paerl, B. Bergman, and E. J. Carpenter (1997), *Trichodesmium*, a globally significant marine cyanobacterium, *Science*, *276*, 1221–1229.

Carlson, C. A. (2002), Production and removal processes, in *Biogeochemistry of Marine Dissolved Organic Matter*, edited by D. A. Hansell and C. A. Carlson, pp. 91–151, Academic, San Diego, Calif.

Chai, F., S. T. Lindley, and R. T. Barber (1996), Origin and maintenance of a high nitrate condition in the equatorial Pacific, *Deep Sea Res., Part II*, *43*, 1031–1064.

Christian, J. R., M. R. Lewis, and D. M. Karl (1997), Vertical fluxes of carbon, nitrogen, and phosphorus in the North Pacific Subtropical Gyre near Hawaii, *J. Geophys. Res.*, *102*, 15,667–15,677.

Christian, J. R., M. A. Verschell, R. Murtugudde, A. J. Busalacchi, and C. R. McClain (2002), Biogeochemical modeling of the tropical Pacific Ocean: II. Iron biogeochemistry, *Deep Sea Res., Part II*, *49*, 545–565.

Coale, K. H., et al. (1996), A massive phytoplankton bloom induced by an ecosystem-scale iron fertilization experiment in the equatorial Pacific Ocean, *Nature*, *383*, 495–501.

Conkright, M. E., et al. (1998), World Ocean Database 1998 CD-ROM data set documentation, *Internal Rep. 14*, Natl. Oceanogr. Data Cent., Silver Spring, Md.

de Baar, H. J. W., and J. T. M. de Jong (2001), Distributions, sources and sinks of iron in seawater, in *The Biogeochemistry of Iron in Seawater*, edited by D. Turner and K. Hunter, pp. 123–253, John Wiley, Hoboken, N. J.

de Baar, H. J. W., J. T. M. de Jong, D. C. E. Bakker, B. M. Löscher, C. Veth, U. Bathmann, and V. Smetacek (1995), Importance of iron for plankton blooms and carbon dioxide drawdown in the Southern Ocean, *Nature*, *373*, 412–415.

Deutsch, C., N. Gruber, R. M. Key, and J. L. Sarmiento (2001), Denitrification and N_2 fixation in the Pacific Ocean, *Global Biogeochem. Cycles*, *15*, 483–506.

Doney, S. C. (1999), Major challenges confronting marine biogeochemical modeling, *Global Biogeochem. Cycles*, *13*, 705–714.

Doney, S. C., D. M. Glover, and R. G. Najjar (1996), A new coupled, one-dimensional biological-physical model for the upper ocean: Applications to the JGOFS Bermuda Atlantic Time-series Study (BATS) site, *Deep Sea Res., Part II*, *43*, 591–624.

Doney, S. C., W. G. Large, and F. O. Bryan (1998), Surface ocean fluxes and water-mass transformation rates in the coupled NCAR climate system model, *J. Clim.*, *11*, 1420–1441.

Doney, S. C., I. Lima, K. Lindsay, J. K. Moore, S. Dutkiewicz, M. A. M. Friedrichs, and R. J. Matear (2001), Marine biogeochemical modeling: Recent advances and future challenges, *Oceanography*, *14*, 93–107.

Doney, S. C., K. Lindsay, and J. K. Moore (2003), Global ocean carbon cycle modeling, in *Ocean Biogeochemistry: A JGOFS Synthesis*, edited by M. Fashom, pp. 217–238, Springer-Verlag, New York.

Dugdale, R. C., and F. P. Wilkerson (1998), Silicate regulation of new production in the equatorial Pacific upwelling, *Nature*, *391*, 270–273.

Dunne, J. P., J. W. Murray, A. K. Aufdenkampe, S. Blain, and M. Rodier (1999), Silicon-nitrogen coupling in the equatorial Pacific upwelling zone, *Global Biogeochem. Cycles*, *13*, 715–726.

Dyhrman, S. T., E. A. Webb, D. M. Anderson, J. W. Moffett, and J. B. Waterbury (2002), Cell-specific detection of phosphorus stress in *Trichodesmium* from the Western North Atlantic, *Limnol. Oceanogr.*, *47*, 1832–1836.

Fung, I. Y., S. K. Meyn, I. Tegen, S. C. Doney, J. G. John, and J. K. B. Bishop (2000), Iron supply and demand in the upper ocean, *Global Biogeochem. Cycles*, *14*, 281–291.

Geider, R. J., H. L. MacIntyre, and T. M. Kana (1998), A dynamic regulatory model of phytoplankton acclimation to light, nutrients, and temperature, *Limnol. Oceanogr.*, *43*, 679–694.

Gent, P. R., and J. C. McWilliams (1990), Isopycnal mixing in ocean circulation models, *J. Phys. Oceanogr.*, *20*, 150–155.

Gent, P. R., F. O. Bryan, G. Danabasoglu, S. C. Doney, W. R. Holland, W. G. Large, and J. C. McWilliams (1998), The NCAR climate system model global ocean component, *J. Clim.*, *11*, 1287–1306.

Gnanadesikan, A. (1999), A global model of silicon cycling: Sensitivity to eddy parameterization an dissolution, *Global Biogeochem. Cycles*, *13*, 199–220.

Gnanadesikan, A., R. D. Slater, N. Gruber, and J. L. Sarmiento (2002), Oceanic vertical exchange and new production: A comparison between models and observations, *Deep Sea Res., Part II*, *49*, 363–401.

Gregg, W., P. Ginoux, P. S. Schopf, and N. W. Casey (2003), Phytoplankton and iron: Validation of a global three-dimensional ocean biogeochemical model, *Deep Sea Res., Part II*, *50*, 3143–3169.

Gruber, N., and J. L. Sarmiento (1997), Global patterns of marine nitrogen fixation and denitrification, *Global Biogeochem. Cycles*, *11*, 235–266.

Hansell, D. A., and R. A. Feely (2000), Atmospheric intertropical convergence impacts surface ocean carbon and nitrogen biogeochemistry in the western tropical Pacific, *Geophys. Res. Lett.*, *27*, 1013–1016.

Holligan, P. M., et al. (1993), A biogeochemical study of the coccolithophore, *Emiliania huxleyi*, in the North Atlantic, *Global Biogeochem. Cycles*, *7*, 879–900.

Hood, R. R., V. J. Coles, and D. G. Capone (2004), Modeling the distribution of Trichodesmium and nitrogen fixation in the Atlantic Ocean, *J. Geophys. Res.*, *109*, C06006, doi:10.1029/2002JC001753.

Hutchins, D. A., G. R. DiTullio, Y. Zhang, and K. W. Bruland (1998), An iron limitation mosaic in the California upwelling regime, *Limnol. Oceanogr.*, *43*, 1037–1054.

Iglesias-Rodríguez, M. D., C. W. Brown, S. C. Doney, J. Kleypas, D. Kolber, Z. Kolber, and P. Falkowski (2002), Representing key phytoplankton functional groups in ocean carbon cycle models: Coccolithophorids, *Global Biogeochem. Cycles*, *16*(4), 1100, doi:10.1029/2001GB001454.

Jansen, H., and D. A. Wolf-Gladrow (2001), Carbonate dissolution in copepod guts: A numerical model, *Mar. Ecol. Prog. Ser.*, *221*, 199–207.

Jickells, T., and L. Spokes (2001), Atmospheric iron inputs to the oceans, in *The Biogeochemistry of Iron in Seawater*, edited by D. Turner and K. Hunter, pp. 85–121, John Wiley, Hoboken, N. J.

Johnson, K. S., R. M. Gordon, and K. H. Coale (1997), What controls dissolved iron concentrations in the World Ocean?, *Mar. Chem.*, *57*, 137–161.

Johnson, K. S., F. P. Chavez, and G. E. Friederich (1999), Continental-shelf sediment as a primary source of iron for coastal phytoplankton, *Nature*, *398*, 697–700.

Johnson, K. S., J. K. Moore, and W. O. Smith (2002), Workshop highlights iron dynamics in ocean carbon cycle, *Eos Trans. AGU*, *83*, 481.

Johnson, K. S., et al. (2003), Surface ocean-lower atmosphere interactions in the Northeast Pacific Gyre: Aerosols, iron, and the ecosystem response, *Global Biogeochem. Cycles*, *17*(2), 1063, doi:10.1029/2002GB002004.

Karl, D., R. Letelier, D. Hebel, L. Tupas, J. Dore, J. Christian, and C. Winn (1995), Ecosystem changes in the North Pacific subtropical gyre attributed to the 1991–92 El Niño, *Nature*, *373*, 230–234.

Karl, D., R. Letelier, L. Tupas, J. Dore, J. Christian, and D. Hebel (1997), The role of nitrogen fixation in biogeochemical cycling in the subtropical North Pacific Ocean, *Nature*, *388*, 533–538.

Karl, D., A. Michaels, B. Bergman, D. Capone, E. Carpenter, R. Letelier, F. Lipschultz, H. Paerl, D. Sigman, and L. Stal (2002), Dinitrogen fixation in the world's oceans, *Biogeochemistry*, *57/58*, 47–98.

Klaas, C., and D. E. Archer (2002), Association of sinking organic matter with various types of mineral ballast in the deep sea: Implications for the

rain ratio, *Global Biogeochem. Cycles*, *16*(4), 1116, doi:10.1029/2001GB001765.
Kustka, A., E. J. Carpenter, and S. A. Sañudo-Wilhelmy (2002), Iron and marine nitrogen fixation: Progress and future directions, *Res. Microbiol.*, *153*, 255–262.
Kustka, A., S. Sañudo-Wilhelmy, E. J. Carpenter, D. G. Capone, and J. A. Raven (2004), A revised estimate of the iron use efficiency of nitrogen fixation, with special reference to the marine cyanobacterium *Trichodesmium spp.* (cyanophyta), *J. Phycol.*, *29*, 12–25.
Lancelot, C., E. Hannon, S. Becquevort, C. Veth, and H. J. W. De Baar (2000), Modeling phytoplankton blooms and carbon export production in the Southern Ocean: Dominant controls by light and iron in the Atlantic sector in Austral spring 1992, *Deep Sea Res., Part I*, *47*, 1621–1662.
Landry, M. R. (1997), Iron and grazing constraints on primary production in the central equatorial Pacific: An EqPac synthesis, *Limnol. Oceanogr.*, *42*, 405–418.
Large, W. G., J. C. McWilliams, and S. C. Doney (1994), Oceanic vertical mixing: A review and a model with a vertical K-profile boundary layer parameterization, *Rev. Geophys.*, *32*, 363–403.
Large, W. G., G. Danabasoglu, S. C. Doney, and J. C. McWilliams (1997), Sensitivity to surface forcing and boundary layer mixing in the NCAR CSM ocean model: Annual-mean climatology, *J. Phys. Oceanogr.*, *27*, 2418–2447.
Leonard, C. L., C. R. McClain, R. Murtugudde, E. E. Hofmann, and L. W. Harding Jr. (1999), An iron-based ecosystem model of the central equatorial Pacific, *J. Geophys. Res.*, *104*, 1325–1341.
Letelier, R. M., and D. M. Karl (1996), Role of *Trichodesmium* spp. in the productivity of the subtropical North Pacific Ocean, *Mar. Ecol. Prog. Ser.*, *133*, 263–273.
Leynaert, A., P. Tréguer, C. Lancelot, and M. Rodier (2001), Silicon limitation of biogenic silica production in the equatorial Pacific, *Deep Sea Res., Part I*, *48*, 639–660.
Loukos, H., B. Frost, D. E. Harrison, and J. W. Murray (1997), An ecosystem model with iron limitation of primary production in the equatorial Pacific at 140°W, *Deep Sea Res., Part II*, *44*, 2221–2249.
Luo, C., N. Mahowald, and J. del Corral (2003), Sensitivity study of meteorological parameters on mineral aerosol mobilization, transport and distribution, *J. Geophys. Res.*, *108*(D15), 4447, doi:10.1029/2003JD003483.
Mahowald, N., and C. Luo (2003), A less dusty future?, *Geophys. Res. Lett.*, *30*(17), 1903, doi:10.1029/2003GL017880.
Mahowald, N., K. Kohfeld, M. Hansson, Y. Balkanski, S. P. Harrison, I. C. Prentice, M. Schulz, and H. Rodhe (1999), Dust sources and deposition during the Last Glacial Maximum and current climate: A comparison of model results with paleodata from ice cores and marine sediments, *J. Geophys. Res.*, *104*, 15,895–15,916.
Mahowald, N., C. Zender, C. Luo, D. Savoie, O. Torres, and J. del Corral (2002), Understanding the 30-year Barbados desert dust record, *J. Geophys. Res.*, *107*(D21), 4561, doi:10.1029/2002JD002097.
Mahowald, N., C. J. Luo del Corral, and C. Zender (2003), Interannual variability in atmospheric mineral aerosols from a 22-year model simulation and observational data, *J. Geophys. Res.*, *108*(D12), 4352, doi:10.1029/2002JD002821.
Martin, J. H. (1990), Glacial-interglacial CO_2 change: The iron hypothesis, *Paleoceanography*, *5*, 1–13.
Martin, J. H., R. M. Gordon, and S. E. Fitzwater (1991), The case for iron, *Limnol. Oceanogr.*, *36*, 1793–1802.
Martin-Jézéquel, V., M. Hildebrand, and M. Brzezinski (2000), Silicon metabolism in diatoms: Implications for growth, *J. Phycol.*, *36*, 821–840.
Measures, C. I., and S. Vink (2001), Dissolved Fe in the upper waters of the Pacific sector of the Southern Ocean, *Deep Sea Res., Part II*, *48*, 3913–3941.
Milliman, J. D. (1993), Production and accumulation of calcium carbonate in the ocean: Budget of a nonsteady state, *Global Biogeochem. Cycles*, *7*, 927–957.
Milliman, J. D., P. J. Troy, W. M. Balch, A. K. Adams, Y. H. Li, and F. T. Mackenzie (1999), Biologically mediated dissolution of calcium carbonate above the chemical lysocline?, *Deep Sea Res., Part I*, *46*, 1653–1669.
Moore, J. K., and M. R. Abbott (2000), Chlorophyll distributions and primary production in the Southern Ocean, *J. Geophys. Res.*, *105*, 28,709–28,722.
Moore, J. K., M. R. Abbott, and J. G. Richman (1999), Location and dynamics of the Antarctic Polar Front from satellite sea surface temperature data, *J. Geophys. Res.*, *104*, 3059–3073.
Moore, J. K., M. R. Abbott, J. G. Richman, and D. M. Nelson (2000), The Southern Ocean at the Last Glacial Maximum: A strong sink for atmospheric carbon dioxide, *Global Biogeochem. Cycles*, *14*, 455–475.
Moore, J. K., S. C. Doney, J. C. Kleypas, D. M. Glover, and I. Y. Fung (2002a), An intermediate complexity marine ecosystem model for the global domain, *Deep Sea Res., Part II*, *49*, 403–462.
Moore, J. K., S. C. Doney, D. M. Glover, and I. Y. Fung (2002b), Iron cycling and nutrient limitation patterns in surface waters of the world ocean, *Deep Sea Res., Part II*, *49*, 463–508.
Nelson, D. M., P. Tréguer, M. A. Brzezinski, A. Leynaert, and B. Quéguiner (1995), Production and dissolution of biogenic silica in the ocean: Revised global estimates, comparison with regional data, and relationship to biogenic sedimentation, *Global Biogeochem. Cycles*, *9*, 359–372.
Nelson, D. M., M. A. Brzezinski, D. E. Sigmon, and V. M. Frank (2001), A seasonal progression of Si limitation in the Pacific sector of the Southern Ocean, *Deep Sea Res., Part II*, *48*, 3973–3995.
O'Neil, J. M. (1999), Grazer interactions with nitrogen-fixing marine cyanobacteria: Adaptation for N-acquisition?, *Bull. Inst. Oceanogr.*, *19*, 293–317.
O'Neil, J. M., C. A. Heil, P. M. Gliber, J. Greenwood, C. A. Miller, and J. G. Greenwood (2004), Nutrient dynamics and plankton community changes associated with a bloom of the pelagic cyanobacterium Trichodesmium, *J. Plankton Res.*, in press.
Orcutt, K. M., F. Lipschultz, K. Gunderson, R. Armoto, A. F. Michaels, A. H. Knap, and J. R. Gallon (2001), A seasonal study of the significance of N_2 fixation by Trichodesmium spp. at the Bermuda Atlantic Time-series Study (BATS) site, *Deep Sea Res., Part II*, *48*, 1583–1608.
Oschlies, A. (2000), Equatorial nutrient trapping in biogeochemical ocean models: The role of advection numerics, *Global Biogeochem. Cycles*, *14*, 655–667.
Oschlies, A. (2001), Model-derived estimates of new production: New results point towards lower values, *Deep Sea Res., Part II*, *48*, 2173–2197.
Oschlies, A., and V. Garçon (1999), An eddy-permitting coupled physical-biological model of the North Atlantic: 1. Sensitivity to advection numerics and mixed layer physics, *Global Biogeochem. Cycles*, *13*, 135–160.
Palmer, J. R., and I. J. Totterdell (2001), Production and export in a global ecosystem model, *Deep Sea Res., Part I*, *48*, 1169–1198.
Price, N. M., B. A. Ahner, and F. M. M. Morel (1994), The equatorial Pacific Ocean: Grazer-controlled phytoplankton populations in an iron-limited system, *Limnol. Oceanogr.*, *39*, 520–534.
Ragueneau, O., et al. (2000), A review of the Si cycle in the modern ocean: Recent progress and missing gaps in the application of biogenic opal as a paleoproductivity proxy, *Global Planet. Change*, *26*, 317–365.
Robertson, J. E., C. Robinson, D. R. Turner, P. Holligan, A. J. Watson, P. Boyd, E. Fernandez, and M. Finch (1994), The impact of a coccolithophore bloom on oceanic carbon uptake in the northeast Atlantic during summer 1991, *Deep Sea Res., Part I*, *41*, 297–314.
Sañudo-Wilhelmy, S. A., et al. (2001), Phosphorus limitation of nitrogen fixation by *Trichodesmium* in the central Atlantic Ocean, *Nature*, *411*, 66–69.
Sarmiento, J. L., R. D. Slater, M. J. R. Fasham, H. W. Ducklow, J. R. Toggweiler, and G. T. Evans (1993), A seasonal three-dimensional ecosystem model of nitrogen cycling in the North Atlantic euphotic zone, *Global Biogeochem. Cycles*, *7*, 417–450.
Sarmiento, J. L., J. Dunne, A. Gnanadesikan, R. M. Key, K. Matsumoto, and R. Slater (2002), A new estimate of the $CaCO_3$ to organic carbon export ratio, *Global Biogeochem. Cycles*, *16*(4), 1107, doi:10.1029/2002GB001919.
Sarmiento, J., et al. (2004), Response of ocean ecosystems to climate warming, *Global Biogeochem. Cycles*, *18*, GB3003, doi:10.1029/2003GB002134.
Schlitzer, R. (2000), Applying the adjoint method for biogeochemical modeling: Export of particulate organic matter in the world ocean, *Geophys. Monogr.*, *114*, 107–124.
Sherr, E., and B. Sherr (1988), Roles of microbes in pelagic food webs: A revised concept, *Limnol. Oceanogr.*, *33*, 1225–1257.
Sieracki, M. E., P. G. Verity, and D. K. Stoecker (1993), Plankton community response to sequential silicate and nitrate depletion during the 1989 North Atlantic spring bloom, *Deep Sea Res., Part II*, *40*, 213–225.
Six, K. D., and E. Maier-Reimer (1996), Effects of plankton dynamics on seasonal carbon fluxes in an ocean general circulation model, *Global Biogeochem. Cycles*, *10*, 559–583.
Straile, D. (1997), Gross growth efficiencies of protozoan and metazoan zooplankton and their dependence on food concentration, predator-prey weight ratio, and taxonomic group, *Limnol. Oceanogr.*, *42*, 1375–1385.
Sunda, W. G., and S. A. Huntsman (1995), Iron uptake and growth limitation in oceanic and coastal phytoplankton, *Mar. Chem.*, *50*, 189–206.

Sunda, W. G., and S. A. Huntsman (1997), Interrelated influence of iron, light, and cell size on marine phytoplankton growth, *Nature*, *390*, 389–392.

Takeda, S. (1998), Influence of iron availability on nutrient consumption ratio of diatoms in oceanic waters, *Nature*, *393*, 774–777.

Tegen, I., and I. Y. Fung (1995), Contribution to the atmospheric mineral aerosol load from land surface modifications, *J. Geophys. Res.*, *100*, 18,707–18,726.

Wu, J. F., W. Sunda, E. A. Boyle, and D. M. Karl (2000), Phosphate depletion in the western North Atlantic Ocean, *Science*, *239*, 759–762.

Yamanaka, Y., and E. Tajika (1996), The role of the vertical fluxes of particulate organic matter and calcite in the oceanic carbon cycle: Studies using an ocean biogeochemical general circulation model, *Global Biogeochem. Cycles*, *10*, 361–382.

Zender, C. S., H. Bian, and D. Newman (2003), Mineral Dust Entrainment and Deposition (DEAD) model: Description and 1990s dust climatology, *J. Geophys Res.*, *108*(D14), 4416, doi:10.1029/2009JD002775.

S. C. Doney, Department of Marine Chemistry and Geochemistry, Woods Hole Oceanographic Institution, MS 25, Woods Hole, MA 02543-1543, USA.

K. Lindsay, Oceanography Section, National Center for Atmospheric Research, P.O. Box 3000, Boulder, CO 80307-3000, USA.

J. K. Moore, Earth System Science, University of California, Irvine, Irvine, CA 92697-3100, USA. (jkmoore@uci.edu)